

# Development of Optically-Controlled “Living Electrodes” with Long-Projecting Axon Tracts for a Synaptic Brain-Machine Interface

Dayo O. Adewole<sup>1,2,3,4</sup>, Laura A. Struzyna<sup>1,2,3,4</sup>, Justin C. Burrell<sup>1,2,3</sup>, James P. Harris<sup>1,2</sup>, Ashley D. Nemes<sup>1,2</sup>, Dmitriy Petrov<sup>1,2</sup>, Reuben H. Kraft<sup>5</sup>, H. Isaac Chen<sup>1,2</sup>, Mijail D. Serruya<sup>2,6</sup>, John A. Wolf<sup>1,2</sup>, D. Kacy Cullen<sup>1,2,3,4,\*</sup>

- (1) Center for Brain Injury & Repair, Department of Neurosurgery, Perelman School of Medicine, University of Pennsylvania, Philadelphia, PA, 19104, USA;
- (2) Center for Neurotrauma, Neurodegeneration & Restoration, Corporal Michael J. Crescenz Veterans Affairs Medical Center, Philadelphia, PA, 19104, USA;
- (3) Department of Bioengineering, School of Engineering and Applied Science, University of Pennsylvania, Philadelphia, PA, 19104, USA;
- (4) Center for Neuroengineering & Therapeutics, University of Pennsylvania, Philadelphia, PA, 19104, USA
- (5) Computational Biomechanics Group, The Pennsylvania State University, University Park, PA, 16802, USA;
- (6) Department of Neurology, Thomas Jefferson University, Philadelphia, PA, 19107, USA.

Number of text pages: 13

Number of Figures: 6

**\*Corresponding author:**

D. Kacy Cullen, Ph.D.

105E Hayden Hall/3320 Smith Walk

Philadelphia, PA 19104

Ph: 215-746-8176 Fx: 215-573-3808

Email: [dkacy@pennmedicine.upenn.edu](mailto:dkacy@pennmedicine.upenn.edu)

## Abstract

For implantable neural interfaces, the functional and clinical outcomes of inorganic microelectrodes are challenged by limitations in specificity and long-term performance. A biological intermediary between micro-electrical devices and the brain may improve specificity and longevity through (1) natural synaptic integration with deep neural circuitry, (2) accessibility on the brain surface, (3) optogenetic manipulation for targeted, light-based readout/control. Accordingly, we have developed implantable “living electrodes”, living cortical neurons and axonal tracts protected within soft hydrogel cylinders, for optobiological monitoring/modulation of brain activity. Here we demonstrate fabrication, rapid axonal outgrowth, reproducible cytoarchitecture, and simultaneous optical stimulation and recording of these tissue engineered constructs *in vitro*. We also present their transplantation, survival, integration, and optical recording in rat cortex as an *in vivo* proof-of-concept for this neural interface paradigm. The creation and characterization of these functional, optically-controllable “living electrodes” are critical steps in developing a new class of optobiological tools for neural interfacing.

## Keywords

Neuromodulation; living scaffolds; neural tissue engineering; cell transplant; biomaterials; regeneration; brain-computer interface; neurodegeneration; optogenetics; synapse

## Introduction

Most devices for neuromodulation (e.g. deep brain stimulation electrodes for Parkinson’s disease) and neural recording (commonly called brain-computer interfaces (BCIs)) work by electrically stimulating or capturing neuronal activity within the brain<sup>1</sup>. These neural interfaces have been developed across a range of medical applications; two significant milestones include cochlear prostheses for the hearing-impaired and thought-driven computer control for people with neuromuscular disorders<sup>1</sup>. Despite these achievements, the clinical impact of more advanced neural interfaces is beset by several underlying functional challenges. Implantable BCIs primarily use inorganic microelectrodes, which often exhibit diminished recording quality over time due to a host of biological factors (e.g. inflammation, neuronal loss, glial scarring) and abiotic biostability issues (including decreasing impedance due to loss of insulation and mechanical failure)<sup>1–5</sup>. In parallel, the effectiveness of electrical neuromodulation is limited by an inability to target specific neurons or neuronal subtypes (e.g. excitatory vs. inhibitory neurons) within the volume of charge injection, as well as the thresholds for both safe and functional therapeutic stimulation<sup>6</sup>. Specificity in neuromodulation may be improved with optogenetics, where inducing the expression of light-sensitive proteins in specific neuronal populations allows these subgroups to be controlled on a wavelength-specific basis through photostimulation. However, the longevity and immune response to viral optogenetic transduction in humans is currently unknown, with non-human primate studies suggesting an elevated immunogenic response<sup>7</sup>. Further, light scattering properties of tissue block precise photostimulation of neurons more than a few hundred microns deep<sup>8</sup>. Deeper tissue is accessible with implantable optical fibers, lenses, or micro-LEDs, yet chronic performance must also address complications from the foreign body response to these materials and overheating of surrounding tissue<sup>9,10</sup>. Across electric and/or optical input-output paradigms, the information transfer bandwidth limits the quality of the neural interface. The ability to address these design challenges – compatibility with the brain, target specificity, and long-term stability – will direct the utility and clinical translation of future neuromodulation and neural recording technologies.

We are advancing a potential solution to these limitations through our existing platform, the micro-Tissue Engineered Neural Network (μTENN). μTENNs are discrete population(s) of neurons connected by long bundles of axons protected within a microscopic hydrogel cylinder (“microcolumn”) (Figure 1)<sup>11,12</sup>. μTENNs were originally developed to reconstruct lost or injured neuroanatomy by approximating the brain’s network-level structure – locally-connected neurons spanned by dense axonal tracts – and

previously demonstrated neuronal survival, maintenance of axonal architecture, and synaptic integration with host neurons following cortical microinjection in rats<sup>11-14</sup>. Experimental evidence and computational network analyses using fluorescent calcium imaging have already demonstrated that bidirectional  $\mu$ TENNs exhibit functional connectivity and the potential for directed information transfer by at least 10 DIV *in vitro*<sup>15</sup>. Here we advance the development of  $\mu$ TENNs into a putative “living electrode”; that is, a self-contained, implantable, axon- and synapse-based conduit for optically-controlled neuronal activity and information transfer to/from the brain. In this approach, the  $\mu$ TENN is implanted at a predetermined depth to form synapses with local neural circuitry and propagate information along  $\mu$ TENN axons to/from an externalized apparatus at the brain surface (Figure 1I-J). Transduction of the  $\mu$ TENN neurons to express optogenetic proteins prior to implant would thus enable light-driven neuromodulation (through photostimulation of the  $\mu$ TENN neurons to influence downstream cortical activity) or monitoring (by recording  $\mu$ TENN neurons as a representation of multiple cortical synaptic inputs) (Figure 1J).

This living electrode approach as described may address multiple functional challenges in current neuromodulation and neural recording strategies. As engineered neural microtissue, living electrodes provide a natural biological substrate for signal transfer between the neural target and the brain surface through synapse formation with host neurons. Further, the wholly organic  $\mu$ TENN may ameliorate the chronic foreign body response as any inorganic materials (e.g. photodiode arrays) are relegated to the brain surface, potentially improving long-term stability (Figure 1J). Combined with the targeting specificity of optogenetic neuromodulation, light-driven living electrodes could provide access to deep neuronal circuitry without the light penetration limitations or potential viral delivery risks of existing optogenetic approaches (as viral transduction is restricted to  $\mu$ TENN neurons prior to implant).

Motivated by these potential benefits, the present work details the biofabrication and characterization of a novel optically-controlled living electrode approach to neural interface. Here, we present the following advancements in  $\mu$ TENN technology as a medium for neural interface: (1) the fabrication of next-generation, neuronal aggregate-based unidirectional (single-aggregate) and bidirectional (dual-aggregate)  $\mu$ TENNs; (2) characterization of their growth and viability across multiple construct parameters; (3) validation of their network formation and maturation over time; (4) optical control and monitoring of optogenetically-active  $\mu$ TENNs *in vitro*; (5) implantation and optical readout of aggregate-based  $\mu$ TENNs in rodent cortex as proof-of-concept for living electrodes; and (6) histological evidence of a modest gliotic response to  $\mu$ TENNs, as well as evidence of neuronal survival, neurite outgrowth, and synaptogenesis with host. Through the successful creation and validation of implantable, optically-controlled, and functional neuron- and axon-based microtissue, these developments represent a notable milestone towards the long-term goal of achieving a biologically-based neural interface that offers improved selectivity and longevity compared to alternative non-organic approaches.

## Materials and Methods

All procedures were approved by the Institutional Animal Care and Use Committees at the University of Pennsylvania and the Michael J. Crescenz Veterans Affairs Medical Center and adhered to the guidelines set forth in the NIH Public Health Service Policy on Humane Care and Use of Laboratory Animals (2015).

## Cortical Neuron Isolation and Culture

Neural cell isolation and culture protocols are similar to that of published work<sup>11,12,16</sup>. Briefly, timed-pregnant rats were euthanized, and the uterus removed. Embryonic day 18 fetuses were transferred from the uterus to cold HBSS, wherein the brains were extracted and the cerebral cortical hemispheres isolated under a stereoscope via microdissection. Cortical tissue was dissociated in 0.25% trypsin + 1mM EDTA at 37°C for 10-12 min, after which the trypsin/EDTA was removed and replaced with 0.15 mg/ml DNase in HBSS. Dissociated tissue + DNase was centrifuged for 3 min at 3000 RPM before the

DNase was removed and the cells re-suspended in serum-free neuronal culture media, composed of Neurobasal® + B27® + Glutamax™ (ThermoFisher) and 1% penicillin-streptomycin.

### Micro-Tissue Engineered Neural Network (μTENN) Fabrication

μTENNs were constructed in a three-phase process (Figure 1A-C). First, agarose microcolumns of a specified geometry (outer diameter (OD), inner diameter (ID), and length) were formed in a custom-designed acrylic mold as described in earlier work (Figure 1A)<sup>13</sup>. The mold is an array of cylindrical channels that allow for the insertion of acupuncture needles (Seirin, Weymouth, MA) to form a void with the annular dimensions (OD x ID) of the microcolumn once assembled. The mold has been fabricated with more precise machining equipment relative to earlier work to improve coaxial alignment of the needles and channels. Molten agarose in Dulbecco's phosphate buffered saline (DPBS) was poured into the mold-needle assembly and allowed to cool (agarose: 3% weight/volume). Once the agarose solidified, the needles were removed and the mold disassembled, yielding hollow agarose microcolumns with a specific outer diameter equal to the size of the channels and inner diameter equal to the outer diameter of the needles. Microcolumns were sterilized via UV light for 30 min and stored in DPBS to prevent dehydration until needed. For these studies, the mold channels were 398 μm in diameter and the acupuncture needles were 180 μm, resulting in microcolumns with a 398 μm OD and a 180 μm ID. Microcolumns were cut to the desired length for each cohort as described below.

Next, primary cortical neurons were forced into spheroidal aggregates (Figure 1C). Early-generation μTENNs were created by seeding microcolumns with dissociated primary cortical neurons, resulting in random clustering and multi-directional axonal growth (Figure 1D-E). The formation of neuronal aggregates prior to seeding provides more precise control over μTENN architecture, enabling the growth of long axonal fascicles spanning the length of the microcolumn (Figure 1F-H). To create aggregates, dissociated cortical neurons were suspended at a density of 1.0 – 2.0 million cells/ml and transferred to an array of inverted pyramidal wells made in PDMS (Sylgard 184, Dow Corning) cast from a custom-designed, 3D printed mold (Figure 1B). Neuron suspensions were then centrifuged in the wells at 200g for 5 min before being incubated overnight at 37°C, 5% CO<sub>2</sub>. This centrifugation resulted in forced aggregation of neurons with precise control of the number of neurons per aggregate/sphere (12 μL cell suspension per well). Pyramidal wells and forced aggregation protocols were adapted from Unguin et al<sup>17</sup>.

Finally, microcolumns were removed from DPBS and excess DPBS removed from the microcolumn channels via micropipette. Microcolumns were then filled with extracellular matrix (ECM) comprised of 1.0 mg/ml rat tail collagen + 1.0 mg/ml mouse laminin (Reagent Proteins, San Diego, CA) (Figure 1C). Unidirectional or bidirectional μTENNs were seeded by carefully placing an aggregate at one (unidirectional) or both (bidirectional) ends of a microcolumn using fine forceps under a stereoscope and confirming aggregate adherence for 45 min at 37°C, 5% CO<sub>2</sub>. Early-generation dissociated μTENNs were fabricated by transferring dissociated cortical neurons into the ECM-filled microcolumn via micropipette as detailed in prior work<sup>11,12</sup>. All μTENNs were grown in neuronal culture media with fresh media replacements every 2 days *in vitro* (DIV).

### Growth Characterization

Several groups of aggregate-based μTENNs were fabricated to assess growth across construct polarities (unidirectional or bidirectional) and lengths (from 2 to 9 mm). In addition, early-generation dissociated μTENNs were generated to compare growth of new aggregate-based μTENNs to those generated using that previous methodology. In total, eight experimental groups were generated: dissociated/2 mm long (LE<sub>DISS,2</sub>) (n = 7), unidirectional/2 mm long (LE<sub>UNI,2</sub>) (n = 6), unidirectional/5 mm long (LE<sub>UNI,5</sub>) (n = 3), bidirectional/2 mm long (LE<sub>BI,2</sub>) (n = 15), bidirectional/3 mm long (LE<sub>BI,3</sub>) (n = 12), bidirectional/5 mm long (LE<sub>BI,5</sub>) (n = 17), bidirectional/7 mm long (LE<sub>BI,7</sub>) (n = 8), bidirectional/9 mm long



(LE<sub>BI,9</sub>) (n = 3). Low sample size for LE<sub>BI,9</sub> was due to cessation of neurite outgrowth prior to 10 DIV without network formation (i.e. not forming inter-aggregate connections).

Phase-contrast microscopy images of  $\mu$ TENNs in culture were taken at 1, 3, 5, 8, and 10 DIV at 10x magnification using a Nikon Eclipse Ti-S microscope, paired with a QIClick camera and NIS Elements BR 4.13.00. Growth rates for each group at specific timepoints were quantified as the change in the length of the longest identifiable neurite divided by the number of days between the current and preceding timepoint. The longest neurites were manually identified within each phase image using ImageJ (National Institutes of Health, MD), and length was measured from the edge of the source aggregate to the neurite tip. To standardize measurements, the edge of the source aggregate identified at 1 DIV was used as the reference point across subsequent timepoints. Growth was measured until axons crossed the length of the column (for unidirectional constructs) or axons crossed the distance between aggregates (for bidirectional constructs). Growth rates were averaged for each timepoint, with the average maximum and minimum growth rates and average crossing time compared across aggregate-based  $\mu$ TENNs with one-way analysis of variance (ANOVA). Post-hoc analyses were performed where necessary with Bonferroni-corrected pairwise comparisons. For reference, planar cultures of cortical neurons (n = 10) were grown in parallel with  $\mu$ TENN cultures, with the longest identifiable neurites measured at 1, 3, and 5 DIV. Single neurites could not be identified at later timepoints due to culture maturation. Axonal outgrowth in planar cultures was taken as the average growth rate across timepoints, which were compared via unpaired t-test.

To identify aggregate-specific growth across the microcolumns, cortical neuronal aggregates were labeled with either green fluorescent protein (GFP) or the red fluorescent protein mCherry via adeno-associated virus 1 (AAV1) transduction (Penn Vector Core, Philadelphia, PA). Briefly, after centrifuging aggregates in the pyramid wells, 1  $\mu$ L of AAV1 packaged with the human Synapsin-1 promoter was added to the aggregate wells (final titer:  $\sim 3 \times 10^{10}$  genomic copies/mL). Aggregates were incubated at 37°C, 5% CO<sub>2</sub> overnight before the media was replaced twice, after which transduced aggregates were plated in microcolumns as described above, each with one GFP<sup>+</sup> and one mCherry<sup>+</sup> aggregate (n = 6). Over multiple DIV, images of the  $\mu$ TENNs were taken on a Nikon A1RSI Laser Scanning confocal microscope paired with NIS Elements AR 4.50.00. Sequential slices of 10-20  $\mu$ m in the z-plane were acquired for each fluorescent channel. All confocal images presented are maximum intensity projections of the confocal z-slices.

## Viability Assessment

To assess neuronal viability in both newly formed and mature networks, unidirectional/5 mm (LE<sub>UNI</sub>) and bidirectional/5 mm (LE<sub>BI</sub>)  $\mu$ TENNs were grown to 10 (immature) and 28 (mature) DIV before staining with a calcein-AM/ethidium homodimer-1 (EthD-1) assay (ThermoFisher). Metabolically active cells convert the membrane-permeable calcein AM to calcein, which fluoresces green ( $\lambda_{exc} \sim 495$  nm;  $\lambda_{em} \sim 515$  nm), while EthD-1 enters membrane-compromised cells and fluoresces red upon binding to nucleic acids ( $\lambda_{exc} \sim 495$  nm;  $\lambda_{em} \sim 635$  nm). Age-matched, two-dimensional cortical cultures were plated on polystyrene and stained to identify differences in survival due to the aggregate-culture method.

Briefly, cultures were gently rinsed in DPBS at the selected time points. A solution of calcein-AM (1:2000 dilution; final concentration  $\sim 2$   $\mu$ M) and ethidium homodimer-1 (1:500;  $\sim 4$   $\mu$ M) in DPBS was added to each culture, followed by incubation at 37°C, 5% CO<sub>2</sub> for 30 min. Following incubation, cultures were rinsed twice in fresh DPBS and imaged at 10x magnification on a Nikon A1RSI Laser Scanning confocal microscope paired with NIS Elements AR 4.50.00. Viability was quantified as the ratio of the total area of calcein-AM<sup>+</sup> cells to the total area of both calcein-AM<sup>+</sup> and ethidium-homodimer<sup>+</sup> cells using ImageJ (National Institutes of Health, MD). Sample sizes for each group were as follows: LE<sub>UNI,5mm</sub> (n = 4, 4); LE<sub>BI,5mm</sub> (n = 7, 4); planar cultures (n = 9, 5) for 10 and 28 DIV, respectively.

## Optical Stimulation, Calcium Imaging, and Optical Recording Analysis

As proof-of-concept validation for the optically-controlled living electrode approach, we established an “all-optical” paradigm enabling the simultaneous optogenetic control and optical monitoring of aggregate-based  $\mu$ TENNs *in vitro*. Cortical neuronal aggregates were transduced with either channelrhodopsin-2 (ChR2) for light-based neuronal activation (“input”) or the genetically encoded fluorescent calcium reporter RCaMP1b for optical readout of neuronal activity (“output”) via adeno-associated virus 1 (AAV1) transduction as described above (Penn Vector Core). 5-6 mm-long bidirectional  $\mu$ TENNs were then plated with one input/ChR2<sup>+</sup> aggregate and one output/RCaMP1b<sup>+</sup> aggregate (n = 5). ChR2 and RCaMP have been investigated and used for all-optical electrophysiology *in vitro* with minimal spectral overlap, reducing the likelihood of false positive responses in RCaMP<sup>+</sup> neurons due to photostimulation of ChR2<sup>+</sup> neurons<sup>18</sup>. At 10 DIV,  $\mu$ TENNs were stimulated via an LED optical fiber positioned approximately 1-3mm above the input aggregate, such that the entire aggregate was illuminated. A Plexon Optogenetic Stimulation System with LED modules for each desired wavelength was used to stimulate the  $\mu$ TENNs (Plexon Inc). Stimulation consisted of a train of ten 100ms pulses (1 Hz) at 465nm, within the excitation spectra of ChR2. Each train was repeated three times for a given LED current amplitude (50, 100, 200, 250, 300 mA); amplitudes corresponded to approximate stimulation intensities of 211, 423, 528, and 634 mW/mm<sup>2</sup> from the tip of the optical fiber and 4.7, 9.3, 18.7, 23.3, and 28.0 mW/mm<sup>2</sup> at the aggregate, respectively. As a control,  $\mu$ TENNs were stimulated as above at 620nm (outside of the excitation spectra of ChR2) at 300 mA/28.0 mW/mm<sup>2</sup>. Recordings of the  $\mu$ TENNs’ output aggregates were acquired at 25-30 frames per second on a Nikon Eclipse Ti microscope paired with an ANDOR Neo/Zyla camera and Nikon Elements AR 4.50.00 (Nikon Instruments).

Following optical stimulation and/or recording, calcium imaging acquisitions were manually reviewed against phase images of the same  $\mu$ TENNs to identify regions of interest (ROIs) containing neurons and background ROIs. Neuronal ROIs were identified as areas clearly containing one or more neuronal cell bodies that exhibited repeated synchronous changes in pixel intensity, although due to the dense packing of the aggregate these ROIs also contained axons. Background ROIs were empty square areas containing no neurons (i.e. only culture media). The mean pixel intensities for each ROI were imported into MATLAB for further analysis via custom scripts (MathWorks Inc). Within MATLAB, the background ROI intensity for each recording was subtracted from active ROIs. Ten such ROIs were randomly selected and averaged to obtain a representative fluorescence intensity trace across each output aggregate. Subsequently, the percent change in fluorescence intensity over time ( $\Delta F/F_0$ ) was calculated for each mean ROI, where  $\Delta F$  equals ( $F_T - F_0$ ),  $F_T$  is the mean ROI fluorescent intensity at time T, and  $F_0$  is the average of the lower half of the preceding intensity values within a predetermined sampling window<sup>19</sup>. The peak  $\Delta F/F_0$  for each train was averaged per  $\mu$ TENN for each of the given stimulation intensities. The average maximum  $\Delta F/F_0$  was then compared across stimulation intensities with a one-way ANOVA, with post-hoc analysis performed where necessary with the Tukey procedure. Additionally, the peak  $\Delta F/F_0$  of the output aggregate under 620nm stimulation was used as a control (620nm being outside of ChR2’s activation spectra) and compared to that under 465nm stimulation at 300 mA/28 mW/mm<sup>2</sup> using an unpaired t-test.

## Immunocytochemistry

To determine whether aggregate-based  $\mu$ TENNs matured and attained the desired network architecture over time,  $\mu$ TENNs were grown and fixed in 4% formaldehyde for 35 min at 4, 10, and 28 DIV (n = 6, 4, and 8, respectively).  $\mu$ TENNs were then rinsed in 1x PBS and permeabilized with 0.3% Triton X100 + 4% horse serum in PBS for 60 min before being incubated with primary antibodies overnight at 4°C. Primary antibodies were Tuj-1/beta-III tubulin (T8578, 1:500, Sigma-Aldrich) to label axons and synapsin-1 (A6442, 1:500, Invitrogen) to label pre-synaptic specializations. Following primary antibody incubation,  $\mu$ TENNs were rinsed in PBS and incubated with fluorescently labeled

secondary antibodies (1:500; sourced from Life Technologies & Invitrogen) for 2h at 18°-24°C. Finally, Hoechst (33342, 1:10,000, ThermoFisher) was added for 10 min at 18°-24°C before rinsing in PBS.  $\mu$ TENNs were imaged on a Nikon A1RSI Laser Scanning confocal microscope paired with NIS Elements AR 4.50.00. Sequential slices of 10-20  $\mu$ m in the z-plane were acquired for each fluorescent channel. All confocal images presented are maximum intensity projections of the confocal z-slices.

### Cortical Implantation and Intravital Calcium Imaging

As proof-of-concept validation for optical living electrodes *in vivo*, bidirectional, approximately 1.5mm-long (n=6) or 5.5mm-long (n=4)  $\mu$ TENNs expressing GCaMP were delivered into the brain via stereotaxic microinjection using similar methodology to that described in prior work<sup>11,12</sup>. Male Sprague-Dawley rats weighing 325-350 grams were anesthetized with isoflurane at 1.0-2.0 liters per minute (induction: 5.0%, maintenance: 1-5-2.0%) and mounted in a stereotactic frame. Meloxicam (2.0 mg/kg) and bupivacaine (2.0 mg/kg) were given subcutaneously at the base of the neck and along the incision line, respectively. The area was shaved and cleaned with betadine solution, after which a small craniotomy was made over the primary visual cortex (V1) (coordinates: -5.0 mm AP,  $\pm$ 4.0 mm ML relative to bregma).  $\mu$ TENNs were carefully loaded into a needle under a dissecting microscope by using fine forceps to gently manipulate the microcolumn into the needle shaft. The needle containing the  $\mu$ TENN was then coupled to a Hamilton syringe and mounted onto a stereotactic arm. To deliver the constructs into the brain without forcible expulsion, the needle was mounted on a micromanipulator and slowly inserted into the cortex to a depth of 1.0 mm such that the dorsal  $\mu$ TENN terminal was left ~500  $\mu$ m above the brain surface. The plunger of the Hamilton syringe was then immobilized while the needle containing the  $\mu$ TENN was slowly raised. This method effectively deposited the  $\mu$ TENN in the wake of the needle withdrawal in order to minimize forces on the preformed neural network. Upon needle removal from the brain, the dorsal aggregate of the  $\mu$ TENN was immersed in artificial cerebrospinal fluid (aCSF) warmed to 37° C. To protect the dorsal  $\mu$ TENN terminal and enable imaging of the  $\mu$ TENN and surrounding tissue, 2 custom-made PDMS rings (5.0 mm OD, 2.0 mm ID, 0.35 mm thickness) were placed over the craniotomy/ $\mu$ TENN and secured to the skull with cyanoacrylate glue. A 3.0 mm-diameter glass coverslip was sandwiched between the 2 rings.

To assess whether  $\mu$ TENN neurons could deliver optical readout following microinjection, animals were anesthetized and mounted on a stereotactic frame for multiphoton calcium imaging of the  $\mu$ TENN neurons following a recovery period; i.e. at 5 and 10 days post-implant.  $\mu$ TENNs were imaged on a Nikon A1RMP+ multiphoton confocal microscope paired with NIS Elements AR 4.60.00 and a 16x immersion objective. Recordings of the  $\mu$ TENNs' dorsal aggregates were taken at 3-5 frames per second, similarly to other intravital work<sup>20</sup>. Post-recording, ROIs of  $\mu$ TENN neurons were manually identified, with the mean pixel intensity of each ROI plotted over time as an aggregate-level measure of neuronal activity. To distinguish neuronal activity from the animal breathing artifact, the fast Fourier transform (FFT) of the mean pixel intensity averaged across 10-15 ROIs was used to identify the frequency peak(s) associated with the observed breathing rate during imaging. Peaks were identified as frequencies whose amplitudes were 2 standard deviations or more than the average amplitude of the Fourier spectra.

### Tissue Harvest and Histology

At one week and one-month post-implant, rats were anesthetized with 150 mg/kg euthasol (Midwest) and transcardially perfused with cold heparinized saline and 10% formalin. After post-fixation of the head overnight, the brain was harvested and stored in PBS to assess  $\mu$ TENN survival and host/ $\mu$ TENN synaptic integration (n = 10). Histology was performed via traditional immunohistology (IHC) and the Visikol clearing method to resolve thicker tissue sections where appropriate.

For traditional IHC, brains were blocked (sagittally for longitudinal  $\mu$ TENN visualization and obliquely for axial  $\mu$ TENN visualization) and cut in 20 or 40  $\mu$ m slices for cryosectioning. For frozen sections, slices

were air-dried for 30 minutes, twice treated with ethanol for three minutes, and rehydrated in PBS twice for three minutes. Sections were blocked with 5% normal horse serum (ABC Universal Kit, Vector Labs, cat #PK-6200) in 0.1% Triton-x/PBS for 30-45 minutes. Primary antibodies were applied to the sections in 2% normal horse serum/Optimax buffer for two hours at room temperature. In longitudinal sections, primary antibodies labeled neurons/axons (rabbit anti-NF200; 1:1000), neurons/dendrites (chicken anti-MAP2; 1:1000), neurons/axons (mouse anti-Tuj1; 1:1000), and/or pre-synaptic terminals (mouse anti-synapsin; 1:1000). In axial sections, primary antibodies labeled microglia/macrophages (rabbit anti-Iba-1; 1:1000) and astrocytes (goat anti-GFAP; 1:1000). Sections were rinsed with PBS three times for five minutes, after which secondary antibodies (1:1000) were applied in 2% normal horse serum/PBS for one hour at room temperature. Sections were counterstained with DNA-specific fluorescent Hoechst 33342 for ten minutes and then rinsed with PBS. After immunostaining, slides were mounted on glass coverslips with Fluoromount-G mounting media.

In the Visikol method, brains were glued to a vibratome mounting block directly in front of a 5% low EEO agarose post (Sigma A-6103) and placed in PBS surrounded by ice. The brain was cut in 100-200  $\mu$ m coronal segments with a Leica VT-1000S vibratome until the  $\mu$ TENN implantation site was approximately 1 mm from the cutting face. Subsequently a single 2 mm section containing the microTENN was cut and placed in PBS (frequency setting: 9, speed: 10). The 2 mm brain section was treated at 4°C with 50%, 70%, and 100% tert-butanol, each for 20 minutes. After the ascending tert-butanol steps, the tissue was removed and placed on a kimwipe to carefully remove any excess reagent. Visikol Histo-1 was applied to the sample for 2 hours at 4°C followed by Visikol Histo-2 for 2 hours at 4°C to complete the clearing process. The sample was placed in a petri dish and a hydrophobic well was drawn around the tissue. Fresh Visikol Histo-2 was applied to completely submerge the tissue, which was then covered by a glass coverslip.

Coverslips containing brain slices were imaged on a Nikon A1RMP+ multiphoton confocal microscope paired with NIS Elements AR 4.60.00 and a 16x immersion objective. A 960-nm laser was used to visualize the  $\mu$ TENNs containing neurons expressing GFP/GCaMP for qualitative observations of neuronal presence, location, and construct architecture post-implant.

## General Statistical Methodology

The Shapiro-Wilk test was used to test data for normality prior to statistical comparisons. Unless otherwise specified, ANOVA was used with post-hoc analyses as appropriate. The threshold for statistical significance was defined in all cases as  $p < 0.05$ . All data are presented as mean  $\pm$  standard error of the mean (s.e.m.).

## Data Availability

The raw datasets that support the findings of this study are available from the corresponding author upon reasonable request.

## Results

The objectives of our current efforts were threefold: (1) to reproducibly fabricate “living electrode” aggregate-based  $\mu$ TENNs and characterize their growth, viability, and network architecture, (2) to demonstrate the ability to control and monitor  $\mu$ TENNs via light, and (3) to determine whether living electrode neurons survive *in vivo* and remain viable for optical monitoring once transplanted in the host cortex.

## Fabrication and Axonal Outgrowth

A fundamental step in the creation of  $\mu$ TENNs-based living electrodes is a fabrication method that enables control and consistency of their structure across preparations. In earlier work,  $\mu$ TENNs were



seeded with dissociated cortical neurons suspended in growth media, which in many cases formed clusters at random throughout the microcolumn interior (Figure 1D-E). By instead inducing the neurons to form spheroidal aggregates prior to their plating, these newly developed aggregate-based  $\mu$ TENNs consistently generated the desired cytoarchitecture of discrete somatic and axonal zones *in vitro* (Figure 1F-H). This macro-level aggregate-based  $\mu$ TENN structure was demonstrably reproducible across both unidirectional and bidirectional polarities and a range of microcolumn parameters (e.g., 2mm – 9mm in length), although, as described below, growth dynamics varied across these design parameters.

In practice, implanted  $\mu$ TENNs may need to integrate with targets several millimeters below the brain surface; as such, a critical milestone was the establishment of long axons in a new three-dimensional (3D) microenvironment, as well as early characterization of these axonal growth dynamics to begin exploring the practical constraints of the aggregate culture method. Qualitatively, phase microscopy revealed healthy and rapid axonal outgrowth across all aggregate-based  $\mu$ TENNs through the ECM core; observed growth rates generally peaked at 3-5 DIV before slowing as unidirectional  $\mu$ TENN axons reached the opposing end (Figure 2A) or bidirectional  $\mu$ TENN axons from opposing aggregates grew towards and along each other (Figure 2B-C). For both  $\mu$ TENN polarities, the maximal growth rate increased with the construct length (Figure 2D), with one-way ANOVA of the average maximum growth rate confirming the LE cohort as a significant effect (F-statistic = 14.1,  $p < 0.0001$ ). The fastest growth rate was observed by bidirectional 9-mm (LE<sub>BI,9</sub>)  $\mu$ TENNs, which reached  $1101.8 \pm 81.1$  microns/day at 3 DIV – nearly 17x the rate of early-generation  $\mu$ TENNs (Figure 2D, F; Supplemental Table 1).

Since the cohort was a statistically significant factor, Bonferroni-corrected pairwise comparisons were run and showed that the average maximum growth rates of the longest cohorts (LE<sub>BI,5</sub>, LE<sub>BI,7</sub> & LE<sub>BI,9</sub>) were indeed statistically higher than those of the shortest cohorts LE<sub>BI,2</sub> & LE<sub>BI,3</sub> ( $p < 0.001$ ), while only LE<sub>BI,9</sub> surpassed the unidirectional cohorts with significance (LE<sub>UNI,2</sub>:  $p < 0.01$ ; LE<sub>UNI,5</sub>:  $p < 0.05$ ) (Figure 2D). In addition, both dissociated  $\mu$ TENNs and control planar neuronal cultures exhibited similar growth rates that were an order of magnitude slower than their aggregate counterparts; peak growth rates were  $61.7 \pm 5.01$  (LE<sub>DISS</sub>) and  $39.1 \pm 20.6$  (CTRL) microns/day, respectively (Figure 2F; Supplemental Table 1).

While the longest  $\mu$ TENNs exhibited the fastest peak growth rates, they took the most time to cross the microcolumn length. In addition, several constructs in the LE<sub>BI,7</sub> and LE<sub>BI,9</sub> cohorts exhibited a decline and eventual cessation of measurable outgrowth before fully forming networks. Similarly, one-way ANOVA and Bonferroni post-hoc analysis of the average crossing time showed that LE<sub>BI,7</sub> and LE<sub>BI,9</sub> axons crossed the length of the microcolumn significantly later than those of LE<sub>UNI,2</sub>, LE<sub>BI,2</sub>, LE<sub>BI,3</sub>, and LE<sub>BI,5</sub> (F-statistic = 12.99,  $p < 0.0001 - 0.05$ ) (Figure 2E). LE<sub>UNI,5</sub> axons did not, on average, fully cross the construct length by 10 DIV (Figure 2F, Supplemental Table 1). Notably, one-way ANOVA of the average *minimum* growth rate did not detect any significant differences across aggregate-based LE groups (F-statistic = 1.17,  $p = 0.332$ ).

### $\mu$ TENN Viability

Neuronal maturation and network development is denoted by a complex interplay of growth, pruning (elimination), and remodeling of synaptic connections as individual neurons form larger networks<sup>21</sup>. For  $\mu$ TENNs, phase/fluorescent images and calcium imaging analyses of bidirectional aggregate-based  $\mu$ TENNs provide structural and functional evidence for the presence of an initial inter-aggregate network by 10 DIV<sup>15</sup>. To assess the impact of network maturation and pruning on neuronal survival in these constructs, unidirectional and bidirectional  $\mu$ TENNs were grown to 10 and 28 DIV. Survival was quantified as the ratio of the summed area of calcein-AM<sup>+</sup> (live) cells to that of all (i.e. both calcein-AM<sup>+</sup> and ethidium homodimer<sup>+</sup>) cells at the specified timepoints, with age-matched planar cultures on polystyrene as controls for the aggregate culture method (Supplemental Figure 1A-F).  $\mu$ TENN neurons



survived up to at least 28 DIV, with qualitative observation of survival out to 40 DIV (Supplemental Figure 1I). Although ANOVA identified the DIV as a significant main effect (F-statistic = 32.21,  $p < 0.0001$ ), the LE/culture group was not a significant factor ( $p > 0.84$ ). The interaction effect was significant ( $p < 0.01$ ), so Bonferroni analysis was used to compare groups at each time point (Supplemental Figure 1G). Survival of planar cultures at 28 DIV (53.6%) was found to be statistically lower than that of LE<sub>UNI</sub> (80.3%) ( $p < 0.05$ ), LE<sub>BI</sub> (84.8%) ( $p < 0.001$ ), and planar cultures (97.7%) ( $p < 0.0001$ ) at 10 DIV (Supplemental Figure 1G). Moreover, planar culture viability at 10 DIV surpassed those of both LE<sub>UNI</sub> (68.1%) and LE<sub>BI</sub> (69.0%) at 28 DIV ( $p < 0.01$ ). Overall, planar cultures exhibited an average 45% reduction in viability from 10 to 28 DIV, while LE<sub>UNI</sub> and LE<sub>BI</sub> showed a 15.2% and 18.6% drop over time, respectively (Supplemental Figure 1H).

## **μTENN Architecture and Synaptogenesis**

To characterize changes in μTENN architecture over time, bidirectional μTENNs were engineered to express GFP and mCherry to track cross-aggregate neurite outgrowth and integration. μTENNs were fixed and immunolabeled to determine the spatial distribution of cell somata/nuclei, axons, and synapses at set timepoints prior to and during network formation (Figure 3). Transducing each aggregate prior to seeding enabled the consistent identification of aggregate-specific projections over time (Figure 3A), even within dense axonal bundles (Figure 3B-D). Confocal images of GFP/mCherry μTENNs revealed that projections from each aggregate made contact and grew along opposing axons towards the opposite aggregate (Figure 3E-G); qualitatively, no gross trends were observed in the extent of physical interaction and integration between the two neuronal populations labeled with either reporter. Immunolabeling of cell nuclei with Hoechst revealed that neuronal somata remained localized almost exclusively to the aggregates across timepoints, which were spanned by long bundles of Tuj-1 expressing axonal projections through the microcolumn lumen (Figure 3H). Synapsin I is expressed at the presynaptic terminals of mature neurons and is involved in the regulation of myriad developmental processes, including the formation and maintenance of synapses – making it a suitable proxy for characterizing the neuronal maturity in culture<sup>22–25</sup>. Immunolabeling revealed highly dense intra-aggregate clusters of axons and synapses within μTENNs at all timepoints, presumably formed upon or shortly after plating (Figure 3I-J). No statistically significant differences in synapsin distribution were identified; however, qualitative observations of synapsin-1 expression showed a moderate increase in synapsin-1<sup>+</sup> puncta within the μTENN aggregates as well as along the axonal tracts within the microcolumn lumen over time (Supplemental Figure 2). Immunolabeling thus suggests that neurons within bidirectional μTENNs reach a mature state, i.e. are capable of both intra-aggregate and inter-aggregate synaptogenesis following axonal growth.

## **Calcium Imaging and Optical Stimulation**

Bidirectional μTENNs expressing the calcium reporter GCaMP6f exhibited spontaneous oscillations at and below the delta band (0.5-5 Hz) in the absence of external stimulation (Figure 5A-B, see Supplemental Movies). These observations reflect earlier findings wherein GCaMP<sup>+</sup> μTENNs demonstrated functional connectivity with strongly correlated oscillations in the delta and theta bands, or 1-8 Hz, across aggregates<sup>15</sup>. The abundance of synapsin expression coupled with synchronicity of oscillation between aggregates further support the conclusion that aggregate-based μTENNs form functional synaptic networks with a coherent structure that may be observed at both the neuron- and aggregate-level.

Bidirectional μTENNs were also engineered to enable light-based stimulation and concurrent calcium imaging *in vitro* by transducing one aggregate with ChR2 and the opposing aggregate with RCaMP (Figure 4C-D). Upon illumination of ChR2<sup>+</sup> (input) aggregates with 465nm light (within the excitation spectrum of ChR2), the opposing RCaMP<sup>+</sup> (output) aggregates exhibited time-locked changes in fluorescence intensity in response (Figure 4E-H). “All-optical” μTENNs were fabricated 5 mm in length with wavelength-separated vectors to reduce the probability of photostimulation artifact. To further

reduce the potential for confound from photostimulation artifact, constructs' input aggregates were illuminated with 620nm light (outside of the ChR2 activation spectrum) of equal intensity to serve as a negative stimulation control. Photostimulation at 620nm induced no readily observable responses; the mean peak  $\Delta F/F_0$  of the output aggregate was significantly greater under 465nm stimulation than 620nm stimulation at 28.0 mW/mm<sup>2</sup> ( $p < 0.05$ ) (Figure 4I). Collectively, these findings suggest that the changes in  $\Delta F/F_0$  under 465nm stimulation reflected synaptically mediated firing of neurons in the output aggregate in response to light-based activation of neurons within the input aggregate. Although there was high variability in  $\Delta F/F_0$  between  $\mu$ TENNs, the percent change in the fluorescence of the output aggregate relative to baseline under optical stimulation could be reproducibly distinguished from endogenous activity across all the  $\mu$ TENNs studied; further, the average maximum  $\Delta F/F_0$  positively correlated with the stimulation intensity (Figure 4I). Overall, these results suggest that photostimulation of the input aggregates resulted in controllable signal propagation and modulation of activity in the associated output aggregates.

### Implantation and Intravital Calcium Imaging

Following *in vitro* characterization, 1.0-1.2 mm aggregate-based  $\mu$ TENNs were fabricated as described above, transduced to express GCaMP6, and implanted in rodent V1 via stereotactic microinjection as a proof-of-concept for living electrode survival and function *in vivo*. Following  $\mu$ TENN delivery, a cranial window was affixed to a custom-build PDMS ring assembly adhered to the surrounding skull to permit repeated noninvasive monitoring of the dorsal  $\mu$ TENN aggregate and surrounding V1 (Figure 5A). This noninvasive imaging was performed using multiphoton microscopy in animals anesthetized using controlled isoflurane delivery with carefully monitored, voluntary respiration. Acute postoperative fluorescent imaging confirmed that the bulk of the dorsal aggregate remained intact at the original implant location (Figure 5B-C). Multiphoton calcium imaging of the dorsal aggregate was performed at 5 and 10 days to avoid potential confounds from the microtrauma of the immediate post-transplant environment affecting neuronal activity. This calcium imaging revealed surviving and active GCaMP<sup>+</sup>  $\mu$ TENN neurons *in vivo*, with transients in GCaMP intensity in the delta band (1-5 Hz) (Figure 5D-F). Putative activity was also present at frequencies below 1 Hz (Figure 5F, inset). Of note, the respiration of the animals caused a consistent artifact in the recorded fluorescence signals resembling a low-frequency oscillation in the baseline fluorescence across all ROIs; however, this respiratory artifact could be readily identified and isolated within the FFT of the time-lapse recordings as a ~0.5-0.7 Hz peak distinct from both the delta band and putative sub-1Hz activity (red band, Figure 5F). Interestingly, the intravital  $\mu$ TENN neuronal activity patterns were similar to those recorded from age-matched non-implanted  $\mu$ TENNs *in vitro*, suggesting that aggregate-based  $\mu$ TENNs retain their network structure over days post-transplant. Longer-term studies will evaluate the utility of  $\mu$ TENNs as an output for neuronal activity as host neurons integrate with the ventral terminus of the network, which would presumably alter the network dynamics.

At one week and one month post-injection in the rodent brain, immunohistochemistry in optically-cleared as well as sectioned tissue revealed that  $\mu$ TENN neurons survived and maintained the preformed somatic-axonal architecture, with GFP<sup>+</sup>/GCaMP<sup>+</sup> cell bodies predominantly localized to the microcolumn terminals and spanned by axonal tracts (Figure 6). Staining for markers of astrogliosis and microgliosis in axial sections revealed only a modest host inflammatory reaction to the  $\mu$ TENNs (Figure 6C). Large, dense clusters of GCaMP<sup>+</sup> cell bodies were found at the dorsal regions of implantation (Figure 6B), with axons and dendrites within the lumen spanning microcolumn (Figure 6D). Dorsal aggregates were observed spreading along the brain surface or further along the microcolumn, putatively due to a cell migration away from the aggregate in order to increase interactions with host tissue (Figure 6B). In some cases, there was also neuronal migration up to several millimeters from the ventral implant location, although the presence and extent of migration varied across implants. In general, there was significant neurite outgrowth from the ventral aggregate of the living electrode, with structural evidence of synapse formation with host neurons (Figure 6E,F).

## Discussion

Microelectrodes—the current gold standard for recordings—have functioned in neural interfaces successfully on the order of months, and less frequently years, in rodents, non-human primates, and human patients<sup>1,26–28</sup>. However, microelectrode-based BCIs generally succumb to a complex combination of abiotic and biological factors (including neuronal loss/migration, gliosis, biofouling, electrode movement, and/or mechanical failure) which impede stability, specificity, and clinical deployment<sup>1–5,29</sup>. Optogenetic strategies for neuromodulation enable more selective stimulation, but must restrict the vector of interest to targeted cells, address the scattering and limited tissue penetration of light, and activate transduced cells without overheating brain tissue<sup>30–33</sup>. Ongoing efforts to minimize inflammation have yielded more compliant electrodes and electrode coatings/co-factors; however, the chronic foreign body response, consequent signal drop, and increase in stimulation thresholds continue to negatively affect current neural interface systems.

μTENNs as living electrodes may present an alternative to conventional microelectrode- or optogenetic-based strategies for neuromodulation/recording with improved biocompatibility, selectivity, and longevity. The integration of living cells as functional device elements is not a new concept, for instance other groups have exploited electroactive bacteria for biosensing applications<sup>34</sup>. Similar efforts to develop biohybrid electronics include the introduction of living neural progenitors (or neural-like PC12 cells) and/or glial support cells into biocompatible hydrogels or hydrogel-polymer composites; these “biosynthetic hydrogels” are then layered to coat metallic electrodes<sup>35–37</sup>. However, the “living electrode” approach presented in this work is distinct as an implantable, anatomically-inspired, 3D engineered microtissue preformed *in vitro* prior to delivery into the brain. This approach uses aggregate-based μTENNs, which are designed to form a relay for biological (i.e. synaptic) interface with existing neuronal circuitry while remaining accessible at the brain surface for optical stimulation (input) or imaging (output). By enabling the segregation of cell bodies (aggregates) and axons in a single structure, these μTENNs may be considered a physical abstraction of the mammalian neural connectome, wherein locally-connected neuronal populations are spanned by long distance axonal pathways.

The work presented here sets a critical foundation in developing aggregate-based μTENNs towards a viable neural interface and provides insight into the experimental milestones needed to scale more long-term translational challenges for similar “living” interfaces. In addition, these constructs consistently generate the connectome architecture described above based on the few design parameters (length, polarity) explored in this work. In reality, the biofabrication method developed for aggregate-based μTENNs provides several degrees of control over their microenvironment through systematic variation of its material (e.g. microcolumn curvature, stiffness, bioactivity), chemical (ECM composition, growth factor gradients), and cellular (phenotype(s), expression) properties. There are thus significant opportunities for aggregate-based μTENNs to serve as a multi-faceted and scalable investigative tool both *in vitro* and *in vivo* for the neuroscience field.

Early growth characterization demonstrated that these next-generation μTENNs, created using forced neuronal aggregation and improved microfabrication techniques, can grow to at least 9mm while maintaining the desired cytoarchitecture. Further, they exhibit accelerated axonal outgrowth and greater longitudinal “bundling” of axons than in early-generation dissociated μTENNs (Figure 1E, H). The observed growth rates for axons in dissociated μTENNs averaged ~60 μm/day over the first 3 days, reflecting growth trends in literature for cortical axons<sup>38,39</sup>. In comparison, the peak axonal growth rates from aggregate-based μTENNs exceeded the rate exhibited by dissociated neurons by two orders of magnitude, with the LE<sub>BI,9</sub> group attaining the remarkable axon extension rate of over 1000 μm/day (Figure 2). Neuronal aggregation likely induced bundled and directed neurite extension, and may positively influence axon-ECM interactions with the collagen and laminin comprising the microcolumn lumen. Other potential factors for such accelerated axonal outgrowth from the neuronal aggregates include the restriction of axonal growth to the microcolumn interior and the lack of synaptic targets

within the microcolumn, which may reduce non-linear axon branching between aggregates and permit more efficient growth cone migration within the lumen<sup>38,41–44</sup>. Although peak growth rates across aggregate-based  $\mu$ TENN groups were positively correlated with  $\mu$ TENN length, their initial growth rates did not vary significantly. This may implicate a critical distance between aggregates below which neuronal processes meet before reaching their maximum growth rates. This distance may be required for the neurons to establish sufficient neurotrophic support and/or upregulate the growth machinery required to reach these speeds.

With respect to neuronal health in aggregates, neuronal attrition from 10 to 28 DIV was ~2.4-3x lower in unidirectional and bidirectional  $\mu$ TENNs than in control planar cultures (Supplemental Figure 1G-H). Established work has shown that neurons exhibit better growth and survival in 3D environments, which more accurately approximate conditions *in vivo*<sup>45</sup>. Similarly, the connectome-inspired 3D microstructure of spheroidal aggregates and axonal bundles appears to provide cortical neurons with the requisite conditions for rapid axonal growth and prolonged viability.  $\mu$ TENNs also demonstrated survival out to at least 40 DIV (Supplemental Figure 1I), enabling more chronic *in vitro* investigations of these dynamics and their mechanisms. Potential subsequent steps include the measuring of neuron health and functionality over time across various cell preparations, neuronal phenotypes, and alternative design parameters.

Beyond axonal growth and survival, another significant outcome was the structural and functional connectivity between aggregates for bidirectional  $\mu$ TENNs. Our biofabrication methodology enabled for aggregate-specific transduction and labeling of individual  $\mu$ TENNs such that we could track structural integration between neuronal populations as the constructs matured (Figure 3A-G).

Immunocytochemistry provided additional evidence of network maturation with the presence and proliferation of synapsin<sup>+</sup> puncta from as early as 4 DIV out to at least 28 DIV (Supplemental Figure 2). As the primary points of contact and communication between neurons, synapses are often used to determine the functional maturity of neuronal networks<sup>25,46</sup>. These results suggest that  $\mu$ TENN neurons in aggregates begin to form synaptic networks soon after plating which mature and expand over time, findings consistent with those in planar cortical cultures<sup>25</sup>. Intra-aggregate synapses presumably dominate the synaptic population before axons span the aggregates to form inter-aggregate synapses. Future structural connectivity studies may build on the aggregate-specific labeling here to characterize intra- and inter-aggregate connectivity with greater resolution.

With respect to functional connectivity, we measured spontaneously generated calcium reporter activity in and across the GCaMP<sup>+</sup> aggregates of bidirectional  $\mu$ TENNs (Figure 4, Supplemental Movies 1 & 2), which consisted predominantly of delta-band oscillations (1-5 Hz). High synchronicity across aggregates has been identified in delta-band oscillations through concurrent network analyses of 1.0-1.2 mm bidirectional GCaMP<sup>+</sup>  $\mu$ TENNs *in vitro*, confirming their functional connectivity and capacity for information transfer<sup>15</sup>. Within “all optical” 5-6 mm  $\mu$ TENNs, neurons in the RCaMP<sup>+</sup> aggregate for optical output displayed similar high-amplitude delta-band activity, with the addition of smaller transients corresponding to photostimulation delivered at the ChR2<sup>+</sup> aggregate for light input (Figure 4G-I, Supplemental Movie 3). The evoked activity was wavelength-dependent, with a positive correlation to stimulus intensity that strongly suggest increased activation of ChR2<sup>+</sup> neurons (Figure 4I). These observations validated the presence of functional, long-distance axonal tracts and synaptic integration between two aggregate populations and, crucially, demonstrate the ability of these constructs to serve as an optically-driven input-output platform for the transmission of information. Variability in the input-output response behavior may be attributed to the stimulation source size and position relative to the aggregate, which as a densely-packed 3D sphere would inherently experience non-uniform illumination. Techniques for more uniform spheroidal photostimulation (e.g. with multiple light sources), or sufficient single-source stimulation to approximate the same (e.g. through depolarization of a critical fraction of ChR2<sup>+</sup> neurons) remains an ongoing objective.



Post-transplant into rat cortex, we observed both delta-band oscillations (similar to those measured *in vitro*) and slow-wave oscillations below 1 Hz in GCaMP<sup>+</sup>  $\mu$ TENN neurons (Figure 5). Slow-wave oscillations have been recorded under anesthesia and during slow-wave sleep, as well as in cortical neuronal cultures *in vitro*<sup>47,48</sup>. Whether the detected <1Hz activity represents a response to cortical synaptic inputs remains beyond the scope of the current manuscript but seems unlikely, given the relatively acute imaging time points. However, the detection of calcium transients in  $\mu$ TENN neurons demonstrates they remain viable post-transplant, while sustained delta-band activity suggests active maintenance of the required network structure for synaptic transmission. A more direct assessment of functional integration over time would comprise longitudinal comparative measurements of intravital  $\mu$ TENN activity and host circuitry.

Histological observations at one week and one month revealed gross preservation of construct architecture and neurite outgrowth at the  $\mu$ TENN terminals (Figure 6), reflecting similar findings with early-generation  $\mu$ TENNs in prior work. Further, colocalization of GCaMP<sup>+</sup> processes with synapsin<sup>+</sup> puncta suggest the structural formation of synapses with the cortex, although more functional validation of these histological implications *in vivo* is required as described above. The information transfer bandwidth of a living electrode-based interface is shaped by the extent of its synaptic integration with the brain. While this may enable highly dense, long-term stability as observed with native synaptic connections, controllability over the targeting of synaptic integration and neuronal migration remains a complex, nontrivial translational challenge that may be addressed through one or more strategies. Potential physical methods include a porous membrane at the ventral microcolumn terminal to restrict neuronal migration while permitting axonal projections between the  $\mu$ TENN and host brain. The  $\mu$ TENN itself may be fabricated with a neuronal phenotype known for its desired synaptogenetic behaviors, or genetically engineered for more controllable synaptogenesis versus widespread outgrowth through the up/downregulation of specific developmental proteins<sup>23,49</sup>. Finally, more direct regulation of the transplant environment may also promote more targeted integration, for instance by introducing or promoting expression of trophic factors implicated in axonal guidance and/or synaptic pruning during development<sup>21,50</sup>. Another key concern for implantable interfaces is the invasiveness of delivery. Combined with well-established stereotactic neurosurgical techniques, the living electrode microcolumns may be further minimized to reduce the microinjection footprint. Additionally, their material properties (e.g. stiffness) and potential co-factors (e.g. anti-inflammatory/growth factor cues) may be tailored against any subsequent foreign body response.

In summary, we have used optogenetic and tissue engineering techniques to create so-called living electrodes – cylindrical, hydrogel-encapsulated neuronal populations linked by functional axonal tracts – and demonstrated their biofabrication and functional validation *in vitro*, as well as their targeted delivery, survival and continued function post-transplant. The results described indicate that aggregate-based  $\mu$ TENNs quickly and consistently form similar functional architecture – important for the biofabrication and scale-up of experimentally useful constructs – which is maintained over weeks *in vitro*. Thus  $\mu$ TENNs may serve as an ideal system for studying neuronal growth, maturation, and network dynamics due to their “abstraction” of mammalian brain connectome into individual units<sup>45</sup>. While the constructs in this study were comprised predominantly of glutamatergic neurons,  $\mu$ TENNs may be seeded with aggregates of different neuronal phenotypes or sources. Within the living electrode paradigm, this may enable the delivery of light-driven, synaptically-transduced neuromodulation *in vivo* for specific clinical effects, for instance neural circuit inhibition or diffuse neurotransmitter release. Multiple distinct  $\mu$ TENNs could also be grown in proximity to form connected assemblies, comprising a modular “building-block” approach to model, manipulate, and characterize systems-level network dynamics across neuronal circuits of mixed cell population and increased pathway complexity *in vitro*. Finally, aggregate-based  $\mu$ TENNs were able to survive, grow, and provide GCaMP-based readout following implantation as proof-of-concept validation for preformed, implantable, biological pathways to



synaptically integrate with, probe and modulate neuronal targets through optical interface on the brain surface. These studies lay the groundwork for more in-depth investigations of the utility of aggregate-based  $\mu$ TENNs as both an experimental tool for *in vitro* modeling, and a translational tool for neural interface following targeted transplant in the cerebral cortex or other anatomical targets.

## Acknowledgements:

**Funding:** Financial support was primarily provided by the National Institutes of Health [BRAIN Initiative U01-NS094340 (Cullen), T32-NS043126 (Harris) & T32-NS091006 (Struzyna)] and the National Science Foundation [Graduate Research Fellowship DGE-1321851 (Adewole)], with additional support from the Penn Medicine Neuroscience Center (Cullen), American Association of Neurological Surgeons and Congress of Neurological Surgeons [Codman Fellowship in Neurotrauma and Critical Care (Petrov)], and the Department of Veterans Affairs [Merit Review I01-BX003748 (Cullen), Merit Review I01-RX001097 (Cullen), Career Development Award #IK2-RX001479 (Wolf) & Career Development Award #IK2-RX002013 (Chen)]. Any opinion, findings, and conclusions or recommendations expressed in this material are those of the authors(s) and do not necessarily reflect the views of the National Institutes of Health, National Science Foundation, or Department of Veterans Affairs.

## Author Contributions:

Conceptualization: D.K.C., J.A.W., M.D.S., H.I.C.; Methodology: D.K.C., D.O.A., L.A.S., J.P.H., A.D.N., J.C.B., D.P., H.I.C., J.A.W.; Formal Analysis: D.O.A.; Investigation: D.O.A., J.C.B.; Resources: R.H.K.; Visualization: D.O.A.; Writing – Original Draft: D.O.A.; Writing – Review & Editing: D.O.A., D.K.C., L.A.S., J.P.H., A.D.N., J.C.B., D.P., R.H.K., H.I.C., J.A.W., M.D.S.; Supervision: D.K.C., J.A.W., M.D.S., R.H.K., H.I.C.; Project Administration: D.K.C.; Funding Acquisition (primary): D.K.C.

## Competing Interests:

D.K.C. is a co-founder of two University of Pennsylvania spin-out companies related to nervous system regeneration and restoration: INNERVACE, Inc. and Axonova Medical, LLC. There are two patent applications related to the methods, composition, and use of micro-tissue engineered neural networks, including U.S. Patent App. 15/032,677 titled “Neuronal replacement and reestablishment of axonal connections” (D.K.C.) and U.S. Patent App. 16/093,036 titled “Implantable living electrodes and methods for use thereof” (D.K.C., J.P.H., J.A.W., H.I.C., and M.D.S.). The other authors declare that they have no competing interests.

## References

- Adewole, D. O., Serruya, M. D., Harris, J. P., Burrell, J. C., Petrov, D., Chen, H. I., Wolf, J. A. & Cullen, D. K. The evolution of neuroprosthetic interfaces. *Crit. Rev. Biomed. Eng.* **44**, 123–152 (2016).
- Tresco, P. A. & Winslow, B. D. The challenge of integrating devices into the central nervous system. *Crit. Rev. Biomed. Eng.* **39**, 29–44 (2011).
- Harris, J. P. & Tyler, D. J. Biological, mechanical, and technological considerations affecting the longevity of intracortical electrode recordings. *Crit. Rev. Biomed. Eng.* **41**, 435–56 (2013).
- Grill, W. M., Norman, S. E. & Bellamkonda, R. V. Implanted neural interfaces: biochallenges and engineered solutions. *Annu. Rev. Biomed. Eng.* **11**, 1–24 (2009).
- Polikov, V. S., Tresco, P. a. & Reichert, W. M. Response of brain tissue to chronically implanted neural electrodes. *J. Neurosci. Methods* **148**, 1–18 (2005).
- Cogan, S. F. Neural stimulation and recording electrodes. *Annu. Rev. Biomed. Eng.* **10**, 275–309

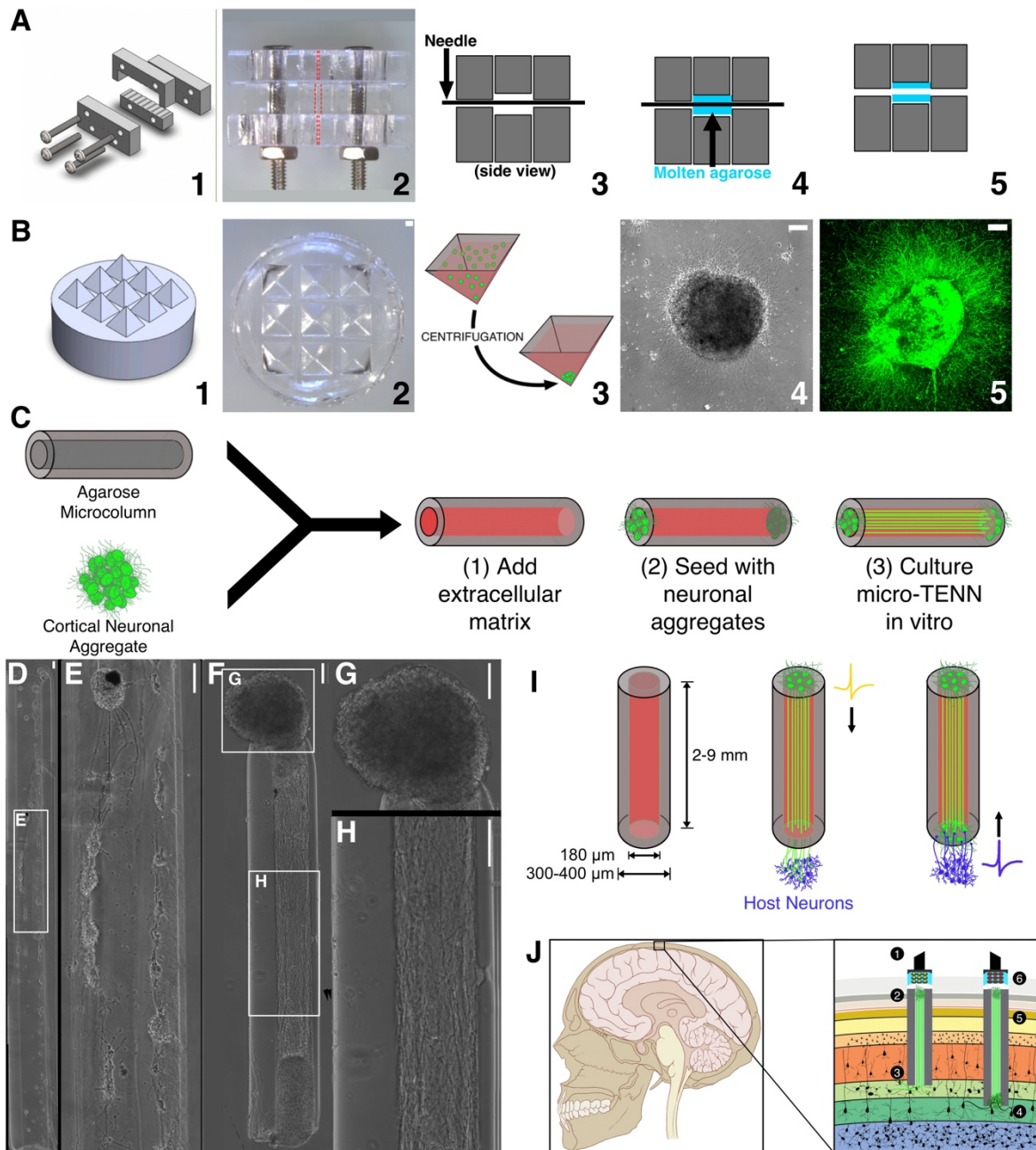
(2008).

7. Mendoza, S. D., El-Shamayleh, Y. & Horwitz, G. D. AAV-mediated delivery of optogenetic constructs to the macaque brain triggers humoral immune responses. *J. Neurophysiol.* **117**, 2004–2013 (2017).
8. Aravanis, A. M., Wang, L.-P., Zhang, F., Meltzer, L. a, Mogri, M. Z., Schneider, M. B. & Deisseroth, K. An optical neural interface: in vivo control of rodent motor cortex with integrated fiberoptic and optogenetic technology. *J. Neural Eng.* **4**, S143–S156 (2007).
9. Pashaie, R., Anikeeva, P., Lee, J. H., Prakash, R., Yizhar, O., Prigge, M., Chander, D., Richner, T. J. & Williams, J. Optogenetic brain interfaces. *IEEE Rev. Biomed. Eng.* **7**, 3–30 (2014).
10. Fan, B. & Li, W. Miniaturized optogenetic neural implants: a review. *Lab Chip* **15**, 3838–55 (2015).
11. Harris, J. P., Struzyna, L. A., Murphy, P. L., Adewole, D. O., Kuo, E. & Cullen, D. K. Advanced biomaterial strategies to transplant preformed micro-tissue engineered neural networks into the brain. *J. Neural Eng.* **13**, 016019 (2016).
12. Struzyna, L. A., Wolf, J. A., Mietus, C. J., Chen, I. H., Smith, D. H., Cullen, D. K., Chen, H. I., Smith, D. H., Cullen, D. K., Adewole, D. O., Chen, H. I., Smith, D. H. & Cullen, D. K. Rebuilding brain circuitry with living micro-tissue engineered neural networks. *Tissue Eng.* **21**, 2744–2756 (2015).
13. Struzyna, L. A., Adewole, D. O., Gordián-Vélez, W. J., Grovola, M. R., Burrell, J. C., Katiyar, K. S., Petrov, D., Harris, J. P. & Cullen, D. K. Anatomically inspired three-dimensional micro-tissue engineered neural networks for nervous system reconstruction, modulation, and modeling. *J. Vis. Exp. JoVE* **2017**, (2017).
14. Struzyna, L. A., Harris, J. P., Katiyar, K. S., Chen, H. I. & Cullen, D. K. Restoring nervous system structure and function using tissue engineered living scaffolds. *Neural Regen. Res.* **10**, 679–685 (2015).
15. Dhobale, A. V., Adewole, D. O., Ho Wing Chan, A., Marinov, T., Serruya, M. D., Kraft, R. H. & Cullen, D. K. Assessing functional connectivity across three-dimensional tissue engineered axonal tracts using calcium fluorescence imaging. (Submitted for publication) (2018).
16. Cullen, D. K., Wolf, J. A., Smith, D. H. & Pfister, B. J. Neural tissue engineering for neuroregeneration and biohybridized interface microsystems in vivo (part 2). *Crit. Rev. Biomed. Eng.* **39**, 243–262 (2011).
17. Ungrin, M. D., Joshi, C., Nica, A., Bauwens, C. & Zandstra, P. W. Reproducible, ultra high-throughput formation of multicellular organization from single cell suspension-derived human embryonic stem cell aggregates. *PLoS One* **3**, (2008).
18. Akerboom, J., Carreras Calderón, N., Tian, L., Wabnig, S., Prigge, M., Tolö, J., Gordus, A., Orger, M. B., Severi, K. E., Macklin, J. J., Patel, R., Pulver, S. R., Wardill, T. J., Fischer, E., Schöler, C., Chen, T., Sarkisyan, K. S., Marvin, J. S., Bargmann, C. I., Kim, D. S., Kügler, S., Lagnado, L., Hegemann, P., Gottschalk, A., Schreiter, E. R. & Looger, L. L. Genetically encoded calcium indicators for multi-color neural activity imaging and combination with optogenetics. *Front. Mol. Neurosci.* **6**, 2 (2013).
19. Patel, T. P., Man, K., Firestein, B. L. & Meaney, D. F. Automated quantification of neuronal networks and single-cell calcium dynamics using calcium imaging. *J. Neurosci. Methods* **243**, 26–38 (2015).
20. Mank, M., Santos, A. F., Drenberger, S., Mrcic-Flogel, T. D., Hofer, S. B., Stein, V., Hendel, T.,

- Reiff, D. F., Levelt, C., Borst, A., Bonhoeffer, T., Hübener, M. & Griesbeck, O. A genetically encoded calcium indicator for chronic in vivo two-photon imaging. *Nat. Methods* **5**, 805–811 (2008).
21. Low, L. K. & Cheng, H.-J. Axon pruning: an essential step underlying the developmental plasticity of neuronal connections. *Philos. Trans. R. Soc. B Biol. Sci.* **361**, 1531–1544 (2006).
22. Ferreira, A., Chin, L. S., Li, L., Lanier, L. M., Kosik, K. S. & Greengard, P. Distinct roles of synapsin i and synapsin ii during neuronal development. *Mol. Med.* **4**, 22–28 (1998).
23. Ferreira, A. & Rapoport, M. The synapsins: beyond the regulation of neurotransmitter release. *Cell. Mol. Life Sci.* **59**, 589–595 (2002).
24. Nikolaev, M. & Heggelund, P. Functions of synapsins in corticothalamic facilitation: important roles of synapsin i. *J. Physiol.* **593**, 4499–4510 (2015).
25. Cullen, D. K., Gilroy, M. E., Irons, H. R. & Laplaca, M. C. Synapse-to-neuron ratio is inversely related to neuronal density in mature neuronal cultures. *Brain Res.* **1359**, 44–55 (2010).
26. Hochberg, L. R., Serruya, M. D., Friehs, G. M., Mukand, J. a, Saleh, M., Caplan, A. H., Branner, A., Chen, D., Penn, R. D. & Donoghue, J. P. Neuronal ensemble control of prosthetic devices by a human with tetraplegia. *Nature* **442**, 164–171 (2006).
27. Gilja, V., Pandarinath, C., Blabe, C. H., Nuyujukian, P., Simeral, J. D., Sarma, A. a, Sorice, B. L., Perge, J. a, Jarosiewicz, B., Hochberg, L. R., Shenoy, K. V & Henderson, J. M. Clinical translation of a high-performance neural prosthesis. *Nat. Med.* **21**, 6–8 (2015).
28. Krüger, J., Caruana, F., Volta, R. D. & Rizzolatti, G. Seven years of recording from monkey cortex with a chronically implanted multiple microelectrode. *Front. Neuroeng.* **3**, 6 (2010).
29. Prasad, A., Xue, Q.-S. S., Sankar, V., Nishida, T., Shaw, G., Streit, W. J. & Sanchez, J. C. Comprehensive characterization and failure modes of tungsten microwire arrays in chronic neural implants. *J. Neural Eng.* **9**, 056015 (2012).
30. Towne, C., Montgomery, K. L., Iyer, S. M., Deisseroth, K. & Delp, S. L. Optogenetic control of targeted peripheral axons in freely moving animals. *PLoS One* **8**, (2013).
31. Scharf, R., Tsunematsu, T., Mcalinden, N., Dawson, M. D., Sakata, S. & Mathieson, K. Depth-specific optogenetic control in vivo with a scalable, high-density pLED neural probe. *Nat. Publ. Gr.* **6**, 28381 (2016).
32. Llewellyn, M. E., Thompson, K. R., Deisseroth, K. & Delp, S. L. Orderly recruitment of motor units under optical control in vivo. *Nat. Med.* **16**, 1161–1165 (2010).
33. Favre-Bulle, I. a, Preece, D., Nieminen, T. a, Heap, L. a, Scott, E. K. & Rubinsztein-Dunlop, H. Scattering of sculpted light in intact brain tissue, with implications for optogenetics. *Sci. Rep.* **5**, 11501 (2015).
34. Zajdel, T. J., Baruch, M., Méhes, G., Stavrinidou, E., Berggren, M., Maharbiz, M. M., Simon, D. T. & Ajo-Franklin, C. M. PEDOT:pss-based multilayer bacterial-composite films for bioelectronics. *Sci. Rep.* **8**, 1–12 (2018).
35. Goding, J., Gilmour, A., Robles, U. A., Poole-Warren, L., Lovell, N., Martens, P. & Green, R. A living electrode construct for incorporation of cells into bionic devices. *MRS Commun.* **7**, 487–495 (2017).
36. Richardson-Burns, S. M., Hendricks, J. L., Foster, B., Povlich, L. K., Kim, D. H. & Martin, D. C. Polymerization of the conducting polymer poly(3,4-ethylenedioxythiophene) (PEDOT) around living neural cells. *Biomaterials* **28**, 1539–1552 (2007).

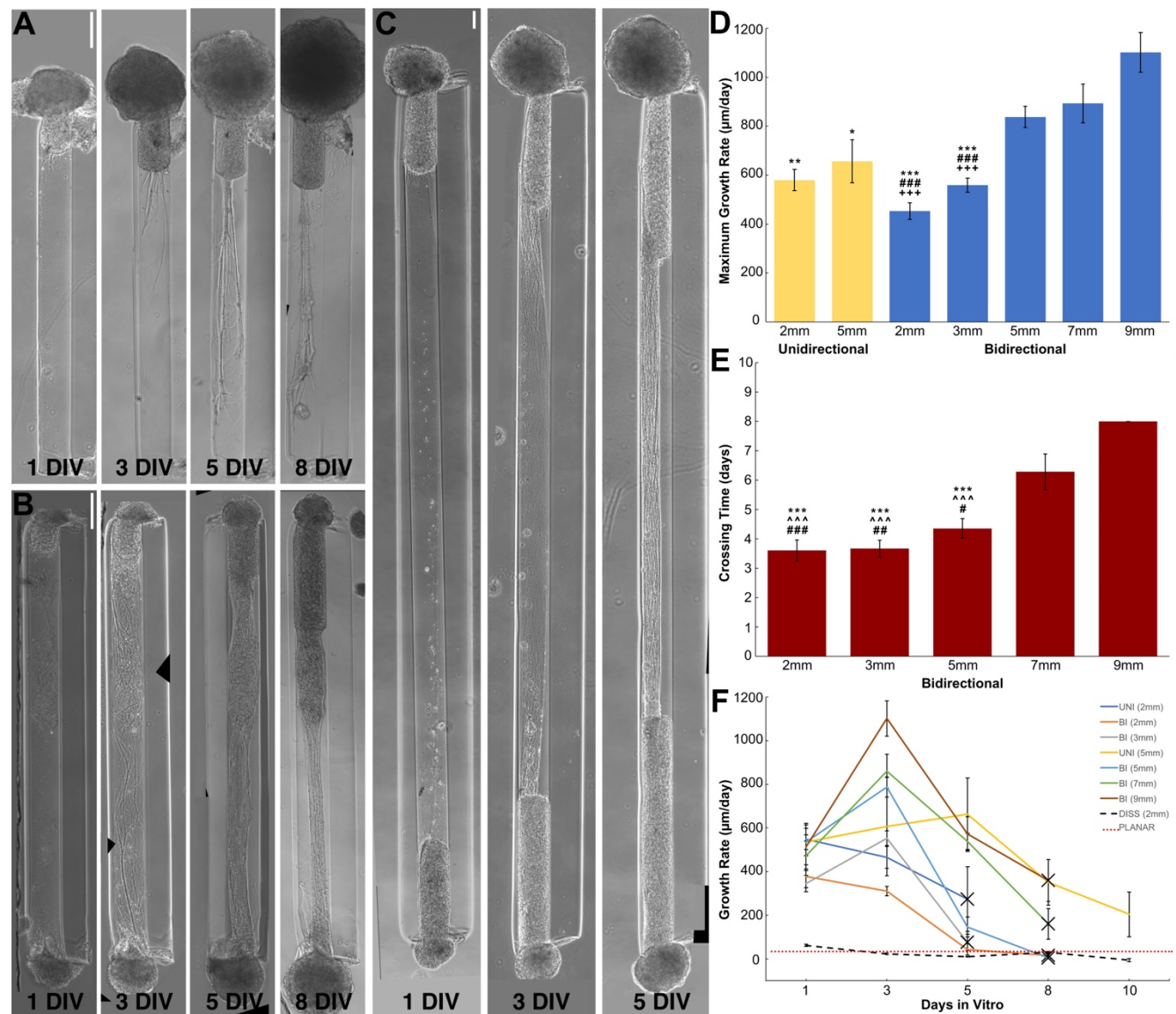
- 825 37. Aregueta-Robles, U. A., Martens, P. J., Poole-Warren, L. A. & Green, R. A. Tissue engineered  
826 hydrogels supporting 3d neural networks. *Acta Biomater.* **95**, 269–284 (2019).
- 827 38. Szebenyi, G., Callaway, J. L., Dent, E. W. & Kalil, K. Interstitial branches develop from active  
828 regions of the axon demarcated by the primary growth cone during pausing behaviors. *J.*  
829 *Neurosci.* **18**, 7930–7940 (1998).
- 830 39. Meberg, P. J. & Miller, M. W. Culturing hippocampal and cortical neurons. *Methods Cell Biol.* **71**,  
831 111–127 (2003).
- 832 40. Goldberg, J. L. How does an axon grow? *Genes Dev.* **17**, 941–958 (2003).
- 833 41. Kalil, K., Szebenyi, G. & Dent, E. W. Common mechanisms underlying growth cone guidance  
834 and axon branching. *J. Neurobiol.* **44**, 145–158 (2000).
- 835 42. Halloran, M. C. & Kalil, K. Dynamic behaviors of growth cones extending in the corpus callosum  
836 of living cortical brain slices observed with video microscopy. *J. Neurosci.* **14**, 2161–2177 (1994).
- 837 43. Tang, F., Dent, E. W. & Kalil, K. Spontaneous calcium transients in developing cortical neurons  
838 regulate axon outgrowth. *J. Neurosci.* **23**, 927–936 (2003).
- 839 44. Kalil, K., Li, L. & Hutchins, B. I. Signaling mechanisms in cortical axon growth, guidance, and  
840 branching. *Front. Neuroanat.* **5**, 1–15 (2011).
- 841 45. LaPlaca, M. C., Vernekar, V. N., Shoemaker, J. T. & Cullen, D. K. Three-dimensional neuronal  
842 cultures. *Methods Bioeng. 3d Tissue Eng.* 187–204 (2010).
- 843 46. Harrill, J. A., Chen, H., Streifel, K. M., Yang, D., Mundy, W. R. & Lein, P. J. Ontogeny of  
844 biochemical, morphological and functional parameters of synaptogenesis in primary cultures of  
845 rat hippocampal and cortical neurons. *Mol. Brain* **8**, 10 (2015).
- 846 47. Franken, P., Dijk, D. J., Tobler, I. & Borbely, A. A. Sleep-deprivation in rats - effects on eeg  
847 power spectra, vigilance states, and cortical temperature. *Am. J. Physiol.* **261**, R198–R208  
848 (1991).
- 849 48. Steriade, M., Nuñez, a & Amzica, F. A novel slow (< 1 hz) oscillation of neocortical neurons in  
850 vivo: depolarizing and hyperpolarizing components. *J. Neurosci.* **13**, 3252–3265 (1993).
- 851 49. Fornasiero, E. F., Bonanomi, D., Benfenati, F. & Valtorta, F. The role of synapsins in neuronal  
852 development. *Cell. Mol. Life Sci.* **67**, 1383–1396 (2010).
- 853 50. Vanderhaeghen, P. & Cheng, H.-J. Guidance molecules in axon pruning and cell death. *Cold*  
854 *Spring Harb. Perspect. Biol.* **2**, (2010).

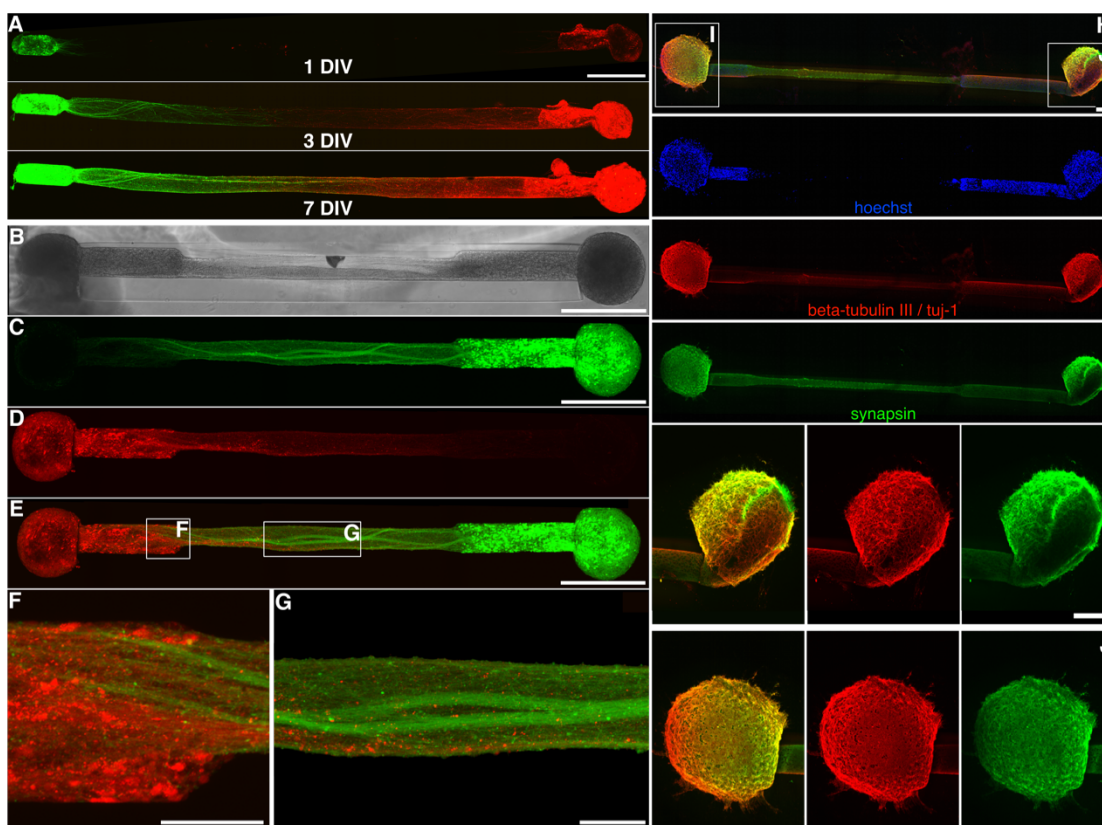




**Figure 1: Aggregate μTENN Fabrication and Living Electrode Concept.** μTENN comprise a hydrogel microcolumn, living neuronal aggregates, and an extracellular matrix lumen. **(A)** 1: A customizable acrylic mold for generating microcolumns. 2: Top view of the mold dashed lines indicate outer diameter (OD; middle) and inner diameter (ID; top & bottom). 3: Needles of the desired inner diameter are inserted into the mold. 4: Microcolumns are cast in agarose (blue). 5: Microcolumns are removed after needle removal & mold disassembly. **(B)** 1: A 3D-printed mold for square pyramidal wells. 2: Pyramidal wells cast in PDMS. 3: Dissociated neurons (green) centrifuged in the wells to form spheroidal aggregates. 4: Phase image of an aggregate 24 hours after plating. 5: Confocal reconstruction of aggregate at 72 hours, labeled with GFP. **(C)** Microcolumns (gray) are filled with an extracellular collagen-laminin matrix (red). Neuronal aggregates are then placed at the microcolumn terminal(s) and grown *in vitro*. **(D)** Early-generation μTENN fabricated with dissociated neurons yielded limited control over the final network structure. **(E)** Aggregate μTENN **(F)** exhibit robust axonal growth and more controllable architecture, with discrete regions of cell bodies **(G)** and neuritic projections **(H)**. **(I)** Left: Current μTENN dimensions for implantable living electrodes. Middle: Unidirectional μTENN synapse host neurons (purple) to relay external inputs to targeted cortical regions. Right: Host neurons synapse bidirectional μTENN, relaying activity from host cortex for monitoring via the dorsal aggregate. **(J)** Optogenetically-active μTENN as transplantable input/output channels. Inputs: an LED array (1) optically stimulates a unidirectional, channelrhodopsin-positive μTENN (2) to activate Layer IV neurons (3). Outputs: Layer V neurons (4) synapse a bidirectional μTENN (5); relayed neuronal activity is recorded by a photodiode array on the brain surface (6). Scale bars: 100 μm.

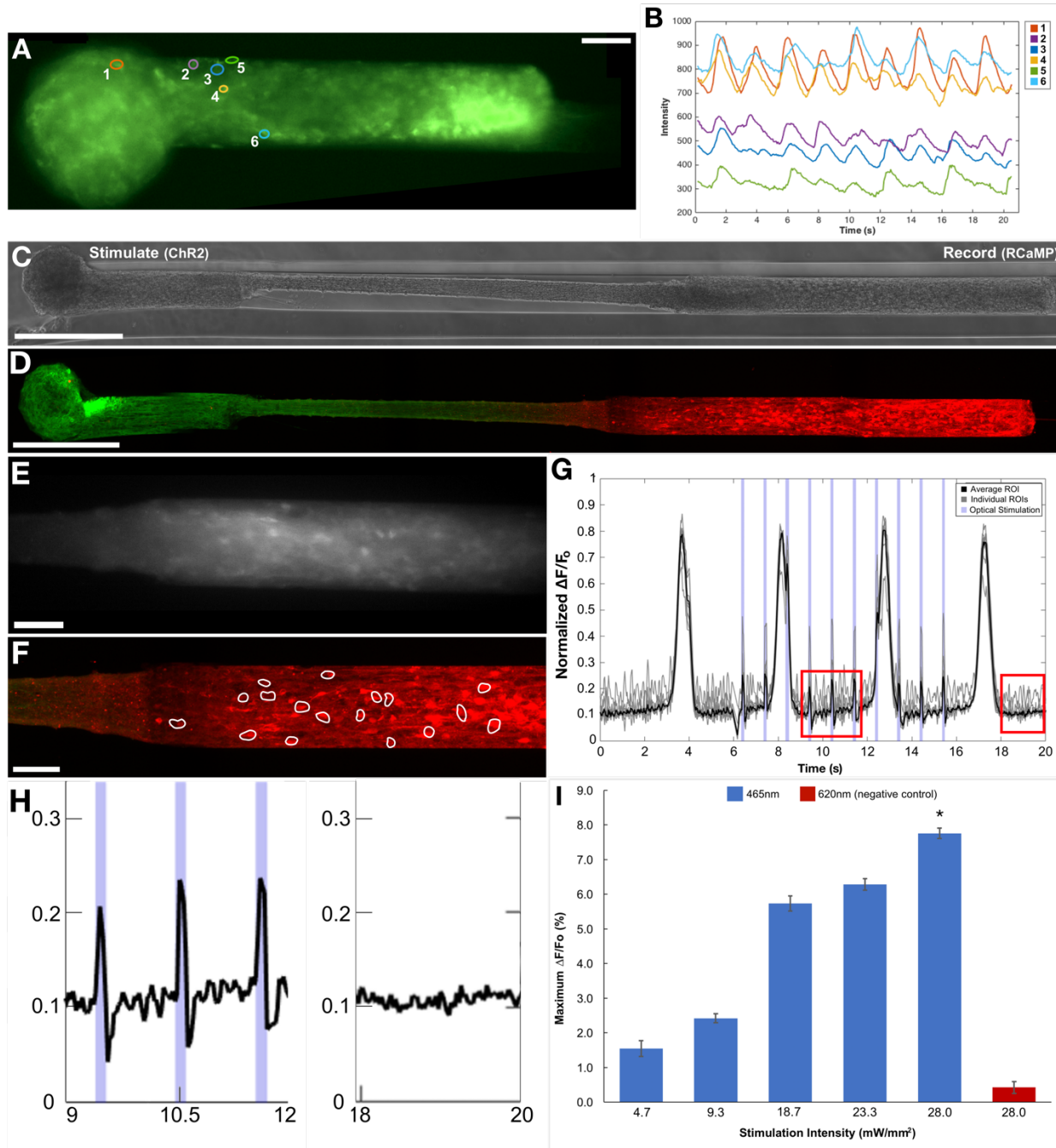






**Figure 3: Aggregate μTENN Architecture.**

Bidirectional μTENN were labeled with GFP (green) and mCherry (red) to observe aggregate-specific axonal growth and structure *in vitro*. (A) Confocal reconstructions of a bidirectional, GFP/mCherry-labeled μTENN at 1, 3 and 7 DIV. (B) Phase image of a bidirectional, GFP/mCherry-labeled μTENN at 5 DIV. (C, D, E) Confocal reconstruction of the μTENN from (B) at 7 DIV, with insets showing axons from each aggregate making contact with the opposing population (F) and growing along each other (G) in the microcolumn lumen. (H) Confocal reconstruction of a representative bidirectional μTENN at 10 DIV, immunolabeled for cell nuclei (Hoechst; blue), axons (beta-tubulin III/tuj-1; red), and synapses (synapsin; green). Cell bodies are localized to the microcolumn terminals with axonal tracts spanning the distance. Insets in (H) refer to callout boxes (I) and (J) showing aggregate zoom-ins of synapses, axonal networks, and their overlay. Scale bars: 500 μm (A-C, E); 100 μm (F, G); 200 μm (H, I).





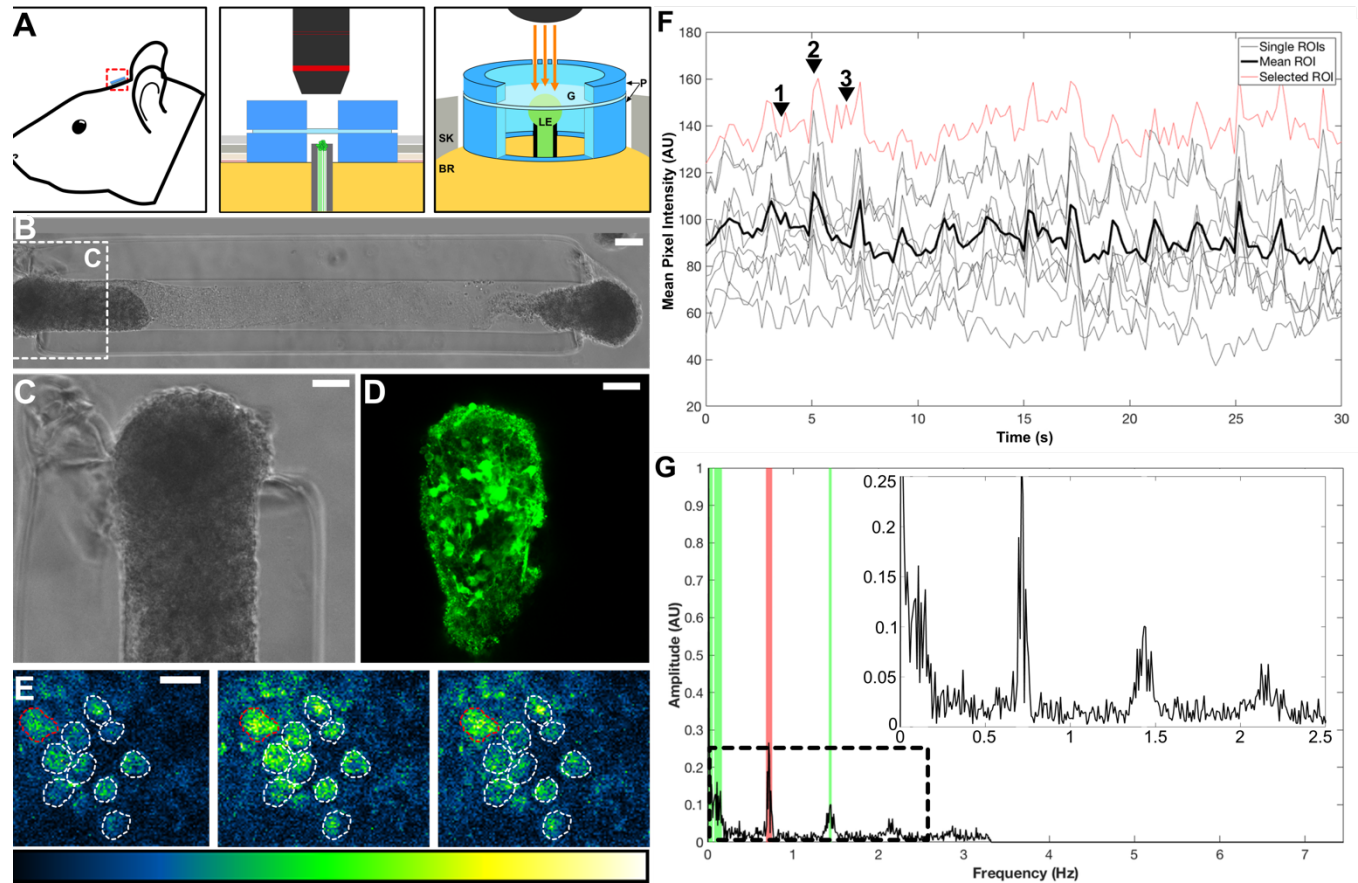


**Figure 5: Living Electrode Function *in Vivo*.**

(A) Conceptual schematic of the living electrode and cranial window, with adjacent zoom-ins (middle & right) showing the PDMS rings (P) sized to the skull craniotomy (SK), securing the glass coverslip (G), and protecting the implanted living electrode (LE) and underlying brain (BR), which may then be imaged chronically (orange arrows). (B) Phase image of a bidirectional GCaMP6s  $\mu$ TENN prior to implant in rodent cortex with a zoom-in (C) of the dorsal aggregate. (D) Multiphoton image of the same dorsal  $\mu$ TENN aggregate acquired immediately post-implant. (E) Single frames from multiphoton recording of the living electrode from (B-D) at 10 days post-implant during low activity (left), breathing (middle), and non-artifact neuronal activity (right). ROIs containing single neurons are outlined. The LUTs scale (0-4096) is provided below. (F) Time course of calcium fluorescence acquisition from (D), showing the individual (grey/red) and mean (black) ROIs. The red trace represents the ROI outlined in red in (E). Numbered arrows denote timestamps from (D). (G) Frequency analysis via Fourier transform of the data from (E), showing spectral peaks due to breathing (red) and neuronal activity (green). Inset shows low-frequency activity similar to that observed *in vitro*. Scale bars: 50  $\mu$ m (B, C); 20  $\mu$ m (D).

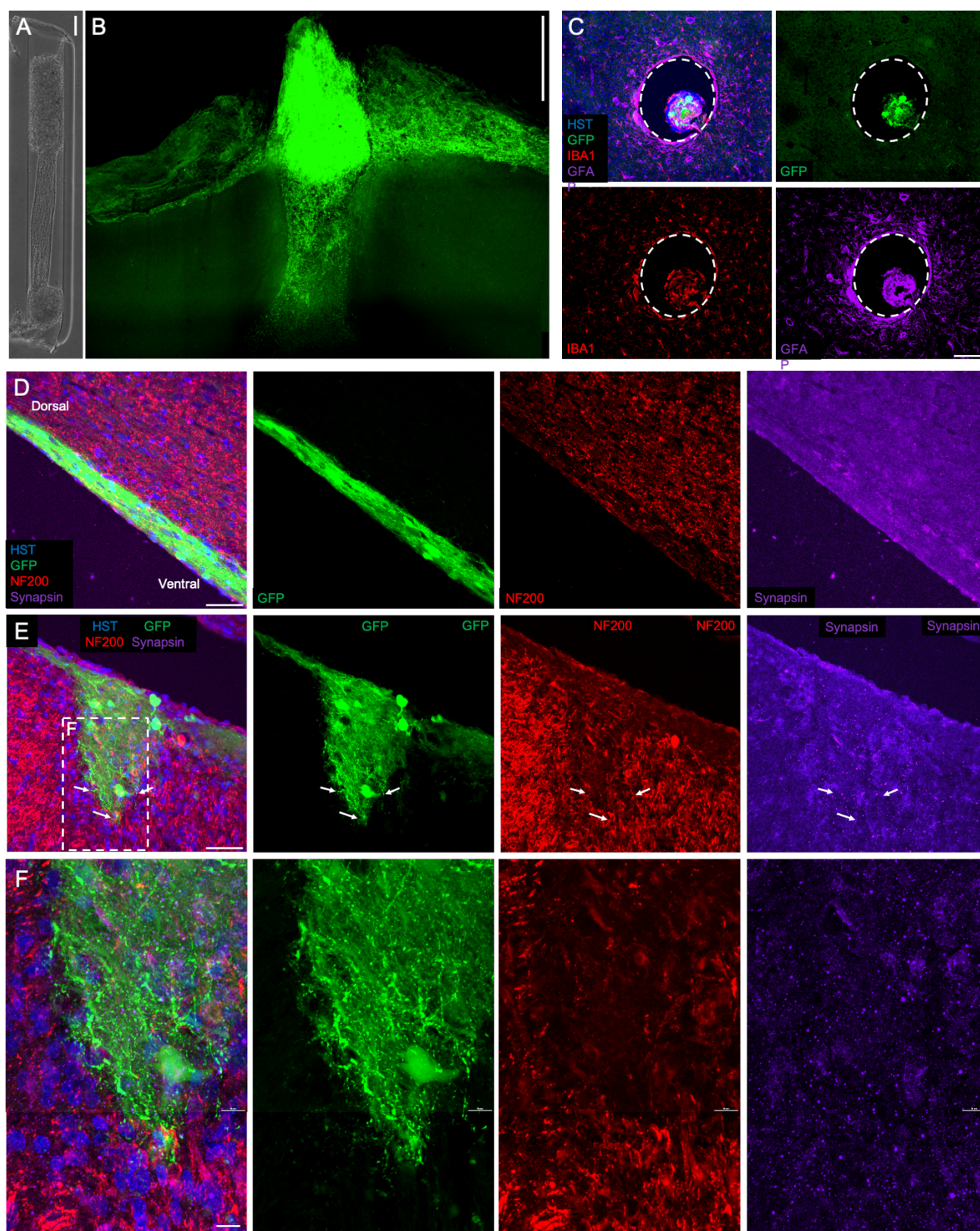


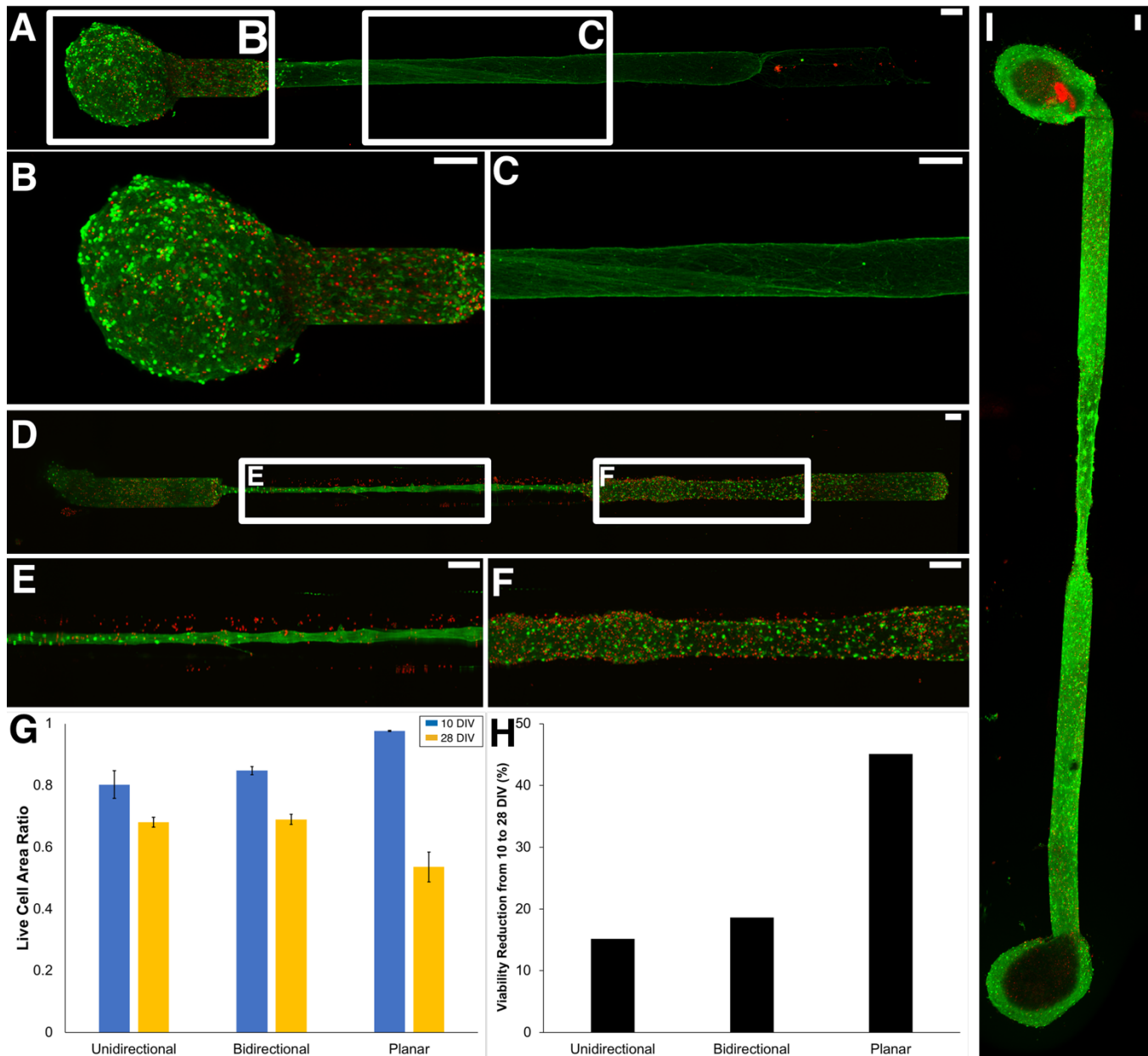
**Figure 6: Living Electrode Survival and Integration *in Vivo*.** (A) Phase image of a bidirectional  $\mu$ TENN prior to implantation; aggregates have been internalized to the microcolumn. (B) Multiphoton image of the  $\mu$ TENN from (f) at one month post-implant, showing GCaMP-positive  $\mu$ TENN neurons and processes within and immediately surrounding the construct. At one month, the dorsal aggregate had descended into the microcolumn, suggesting externalized aggregates may



be required to maintain a cohesive neuronal population at the surface. **(C)** Axial view of implant showing  $\mu$ TENN neurons/axons in the lumen at one month post-transplantation. To visualize the extent of the inflammation response at 1 month following delivery, sections orthogonal to the transplantation site were stained for microglia/macrophages (Iba-1, red) and astrocytes (GFAP, far red). Minimal host neuroinflammatory response was observed at this time point surrounding the implanted construct. Dashed lines denote the host brain- $\mu$ TENN interface. **(D-F)** Longitudinal view of implanted  $\mu$ TENN within the corticothalamic tract at one month post-transplantation, with evidence the construct retained its axonal tracts and overall axo-somatic architecture (GFP, green). **(E)**  $\mu$ TENN neurons and axons (GFP, green) were found projecting ventrally with neurons and neurites interfacing with host tissue at the (deep) ventral end. GFP positive  $\mu$ TENN neurons were visualized in discrete regions with axons extending within the lumen parallel to the cortical-thalamic axis. These findings demonstrate that following stereotaxic microinjection, aggregate  $\mu$ TENNs survive, with neurite extension and integration out to at least 1 month *in vivo*. Arrows denote  $\mu$ TENN neurites penetrating the host brain and putative synapse formation, with dashed inset representing zoom-in **(F)**. Scale bars: 100  $\mu$ m (A-C); 50  $\mu$ m (D, E); 10  $\mu$ m (F).

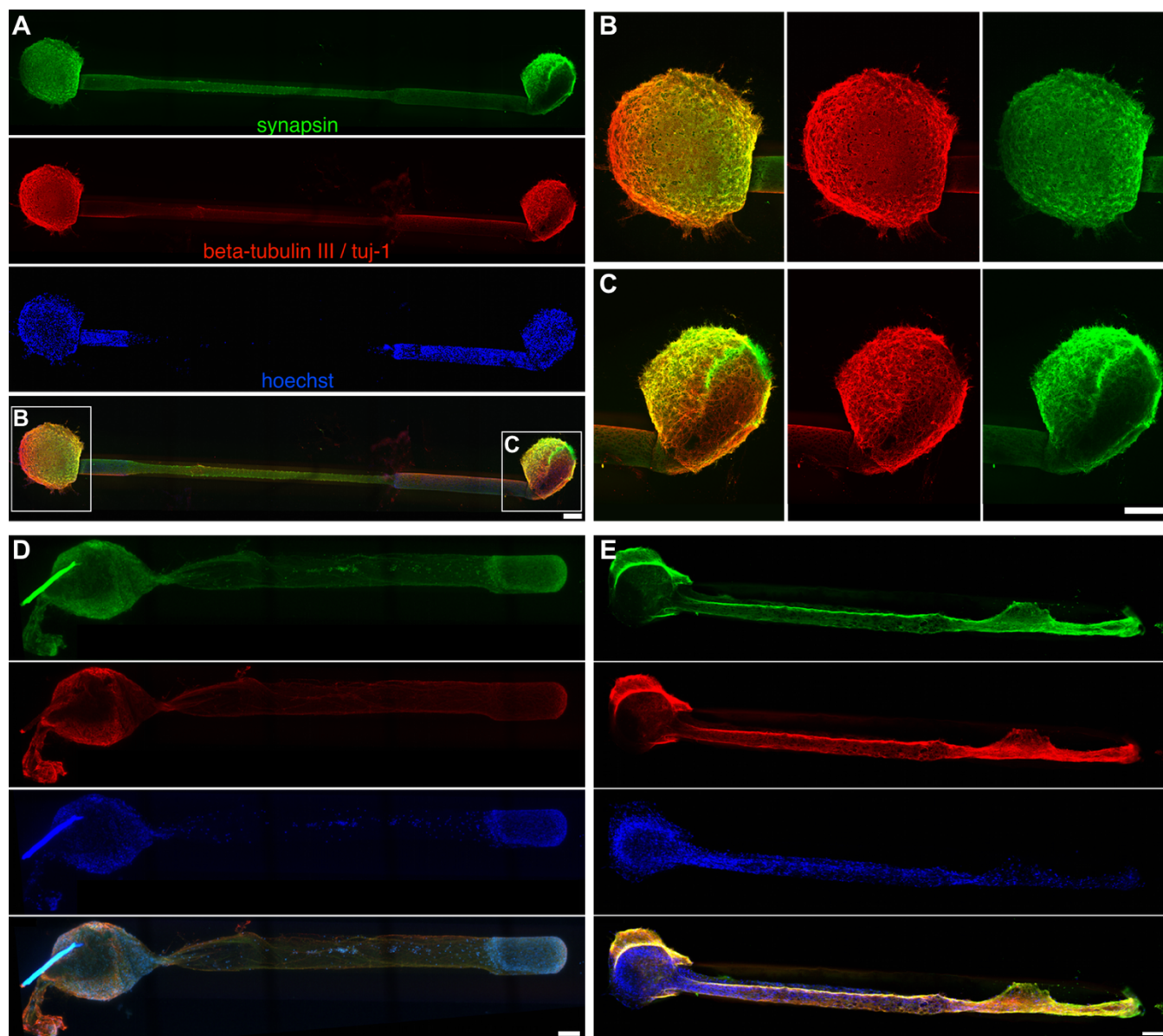
	LE-UNI		LE-BI					DISS	CTRL
	2mm	5mm	2mm	3mm	5mm	7mm	9mm	2mm	N/A
<b>Initial Rate</b>	547±73.2	525±21.9	378±51.9	345±35.4	535±62.9	472±66.9	513±100	61.7±5.01	38.1±19.4
<b>Max Rate</b>	580±43.9	656±88.3	453±33.8	559±28.7	838±43.2	894±79.2	1102±81	61.7±5.01	39.1±20.6
<b>Min Rate</b>	430±73.0	202±74.9	248±22.7	324±38.0	395±56.4	336±57.4	313±68.3	-5.37±7.50	38.1±19.4
<b>Crossing Time</b>	4.33	N/A	3.60	3.67	4.35	6.29	8.0	N/A	N/A

**Supplemental Table 1:  $\mu$ TENN Growth Characterization.** Initial, Maximum, and Minimum Rates of axonal growth are in units of microns/day, while Crossing Times for  $\mu$ TENN axons are in units of days in vitro. Column headers indicate unidirectional (LE-UNI), bidirectional (LE-BI), dissociated (DISS)  $\mu$ TENNs, or planar control cultures (CTRL), with subheaders indicating  $\mu$ TENN length where appropriate. All data are presented as mean  $\pm$  s.e.m.



### Supplemental Figure 1: $\mu$ TENN Viability.

Viability for unidirectional and bidirectional  $\mu$ TENNs and age-matched two-dimensional controls was quantified via live-dead (calcein-AM/ethidium homodimer) staining at 10 and 28 DIV. **(A-C)** Representative confocal live-dead images showing live cells (green), dead cells (red), and an overlay of a unidirectional  $\mu$ TENN at 10 DIV, with outlined insets below. **(D-F)** Representative confocal live-dead image of a bidirectional  $\mu$ TENN at 28 DIV, with outlined insets below. **(G)** The average proportion of live to total (live + dead) cell body area for each experimental group and timepoint. Two-way ANOVA and post-hoc analysis revealed several statistically relevant pairwise differences (\* =  $p < 0.05$ ; \*\* =  $p < 0.01$ ; \*\*\* =  $p < .001$ ). Symbols denote significant differences vs. planar cultures at 10 DIV (#) and 28 DIV (\*). Error bars denote s.e.m. Sample sizes:  $n = 4$  and  $4$  (unidirectional);  $7$  and  $4$  (bidirectional);  $9$  and  $5$  (controls) for 10 and 28 DIV, respectively. **(H)** The percent change in viability across experimental groups. All groups showed a decline in viability, with the planar cultures nearing a three-fold drop in viability relative to the  $\mu$ TENNs out to 28 DIV. **(I)** Live-dead stain of a  $\mu$ TENN at 40 DIV. Scale bars:  $100\ \mu\text{m}$ .



**Supplemental Figure 2: Visualizing  $\mu$ TENN Architecture over Time.**  
**(A-C)** Reproduction of Figure 3 from the main text, compared to representative  $\mu$ TENN at 4 DIV **(D)** and 28 DIV **(E)**. Immunolabeling remains consistent, with cell nuclei (Hoechst; blue), axons (beta-tubulin III/tuj-1; red), and synapses (synapsin; green). Scale bars: 200  $\mu$ m (A, C); 100  $\mu$ m (D, E).



**Supplemental Video 1 & 2: Calcium Imaging within  $\mu$ TENNs.**

The two videos show spontaneous network activity within  $\mu$ TENN aggregates, visualized with the genetically encoded calcium reporter GCaMP6f. Video 1 shows the same  $\mu$ TENN aggregate shown in Figure 4A. Video 2 shows a bidirectional  $\mu$ TENN approximately 2mm in length, imaged at 9 days in vitro. Note that GCaMP activity can be seen in both the aggregate and axonal regions of the  $\mu$ TENN.

**Supplemental Video 3: Simultaneous Optical Stimulation & Calcium Imaging within  $\mu$ TENNs.**

A short sample from an acquisition of the “all-optical” photostimulation & calcium recording described in Figure 4. An RCaMP<sup>+</sup> aggregate is in the field of view while the ChR2<sup>+</sup> aggregate is pulsed with light (red arrows) at gradually increasing intensities.